Electrochimica Acta 526 (2025) 146195

Contents lists available at ScienceDirect

Electrochimica Acta

journal homepage: www.journals.elsevier.com/electrochimica-acta

# $WO_3/BiVO_4$ heterojunctions: Photoelectrochemical performance for dexamethasone degradation and toxicity assessment in *Lactuca sativa*

Roberta Y.N. Reis [a], Isabelle M.D. Gonzaga [a], Roger Gonçalves [a], Carlos H.M. Fernandes [b], Marcelo Assis [c], Ernesto C. Pereira [a], Marcos R.V. Lanza [b], Lucia H. Mascaro [a,*]

[a] *Universidade Federal de São Carlos, Rod. Washington Luiz, Km 235, São Carlos, SP 13565-905, Brazil*
[b] *São Carlos Institute of Chemistry, University of São Paulo, 400 São Carlos, SP 13566-590, Brazil*
[c] *Biomaterials and Tissue Engineering Laboratory, Federal University of São Paulo - UNIFESP, Santos, SP 11015-020, Brazil*

ARTICLE INFO

*Keywords:*
Photoelectrocatalysis
Heterostructures
Dexamethasone
$WO_3$
$BiVO_4$
Toxicity

ABSTRACT

Water contamination by dexamethasone (DEX) poses a significant threat to the global population. Developing an effective and affordable system for DEX removal remains a critical need, particularly in treating DEX and other contaminants at environmentally relevant concentrations. Chemical bath and spin coating techniques were applied to synthesize a custom-designed $WO_3/BiVO_4$ interface electrode on a fluorine-doped tin oxide (FTO) substrate. Each $WO_3/BiVO_4$, $WO_3$, and $BiVO_4$ layer was characterized both photochemically and electrochemically to identify enhanced light harvesting and electron transfer at the heterojunction. Compared to the pristine materials, more charge carriers, enhanced transfer, and separation of photogenerated pairs were observed. The effectiveness of the $WO_3/BiVO_4$ electrode in removing 10 mg $L^{-1}$ DEX was evaluated under photolysis, electrocatalysis (EC), and photoelectrocatalysis (PhEC) treatment conditions. The PhEC treatment at 1 mA $cm^{-2}$ under visible light irradiation exhibited an excellent DEX removal efficiency of 100 %, surpassing photocatalysis (54 %) and EC (14.6 %). The mineralization rate and the formation of short-chain acids (oxalic, succinic, glycolic, and adipic) depended on the processes investigated. The large formation of superoxide radicals from the photogenerated charges in $WO_3/BiVO_4$ was revealed by scavenger tests, elucidating the degradation mechanism in PhEC, which resulted in a final product with lower toxicity, proven by tests with *Lactuca sativa*. The application of reuse cycles and characterizations after the PhEC processes demonstrated the electrode's good quality and useful life. Therefore, it can be inferred that the $WO_3/BiVO_4$ electrode applied in the PhEC process efficiently removes DEX and presents itself as a promising proposal for treating residual drugs in environmental matrices.

## 1. Introduction

Recalcitrant compounds in water are already a reality in various countries worldwide [1]. Among the several compounds detected in water sources, pharmaceutical compounds of other classes, such as antibiotics, fungicides, analgesics, and anti-inflammatories, have raised great concern in the scientific community due to the nature of these compounds and their difficult elimination [2,3]. Faced with this problem, the UN proposed 17 Sustainable Development Goals (17 SDGs) to be achieved by 2030, with environmental and climate protection among the several goals [4]. In this context, the scientific community has been tasked with developing water treatment technologies that can effectively address various contaminants to achieve this goal. Water contamination by anti-inflammatories substantially threatens human health and the environment [5]. A massive volume of drugs has been used for the diagnosis and treatment of diseases. This use has intensified in the last four years due to the pandemic and the increase in acute respiratory diseases, given the recalcitrant nature of these compounds and the metabolites that can be generated after human consumption and subsequent excretion [6,7].

In this context, dexamethasone is a corticosteroid that has become widely used. It belongs to the therapeutic class of anti-inflammatory drugs effective for treating respiratory diseases, allergies, and inflammation, which results in its recurrent presence in water bodies [8]. One of the significant concerns regarding DEX and other drugs is the ineffectiveness of treating these compounds in conventional wastewater treatment plants (WWTPs) using traditional processes that often tend to generate products with higher toxicity than the original compounds,

---

[*] Corresponding author.
*E-mail address:* lmascaro@ufscar.br (L.H. Mascaro).

https://doi.org/10.1016/j.electacta.2025.146195
Received 26 December 2024; Received in revised form 16 February 2025; Accepted 3 April 2025
Available online 4 April 2025
0013-4686/© 2025 Elsevier Ltd. All rights are reserved, including those for text and data mining, AI training, and similar technologies.

thus making it necessary to search for effective water treatment methods that can guarantee the elimination of recalcitrant compounds from water. Several recent studies have been conducted using advanced oxidation processes (AOPs) for treating refractory organic compounds from wastewater [9]. Since it considers its ability to promote the complete mineralization of pollutants with little or no generation of waste/by-products [10]. The AOPs rely on producing potent oxidizing agents, with the hydroxyl radical ($^{\bullet}OH$) being particularly notable due to its exceptional reactivity as an oxidizing agent. ($E^{\circ} = 2.8$ V vs. $E$=SHE – standard hydrogen electrode) [11].

Among the AOPs, the photoelectrocatalytic process (PhEC) is attractive for mineralization and contaminant removal. This technology involves the application of immobilized semiconductor materials in the form of films. When irradiated and under a polarization potential, these materials generate charge carriers ($e^{-}/h^{+}$) in the reaction medium, which are available for oxidation processes. Additionally, it is an environmentally friendly and cost-effective technology [12–14]. The designed use of PhEC can provide several advantages for DEX removal, including adsorption and oxidation of the species and lower energy consumption. In this process, water treatment involves the electro-generated oxidants (such as $^{\bullet}OH$ and $^{\bullet}O_2^{-}$), which react with organic pollutants to degrade them. Different metal oxides have been used as photoactive electrodes, such as $TiO_2$ [15], ZnO [16], CuO [17], $Fe_2O_3$ [18], $BiVO_4$ [19], and $WO_3$ [20], among others—however, these materials alone often present undesirable characteristics, such as low sunlight absorption rate and photocorrosion. Photoelectrocatalyst engineering is an alternative to overcome this limitation. The union of two or more metal oxides can provide heterostructures with improved synergistic performance. Combining these materials can effectively result in heterostructures with improved charge separation rates and greater efficiency in generating strong oxidants, thus promoting more efficient degradation and mineralization of refractory organic compounds in water [21]. The formation of heterostructures with n-type semiconductors such as $WO_3$ and $BiVO_4$ provides a combination in the valence (VB) and conduction (CB) bands of these semiconductors, allowing the suppression of charge recombination, improved separation of photogenerated charge, as well as increased lifetime of charge carriers, as already proven in other studies [22–24]. Lee et al. [21] demonstrated through the study of different heterojunctions with $BiVO_4$ that combining it with $WO_3$ makes achieving high current densities possible, thereby increasing the incident photon conversion efficiency and improving light capture in the visible region.

The high photoelectrochemical performance of the $WO_3/BiVO_4$ heterojunction is attributed to the fact that both materials, $WO_3$ and $BiVO_4$, are photoanodes with good chemical stability, narrow band gap ($WO_3$ $E_g = 2.5$–$2.7$ eV, $BiVO_4$ $E_g = 2.4$ eV) and can be applied for clean energy conversion and contaminant removal [25]. In this context, we synthesized a $WO_3/BiVO_4$ heterojunction through two simple chemical bath steps, followed by spin-coating deposition, for the photoelectrochemical degradation of DEX in simulated effluent. The need for studies that address the photoelectrochemical degradation of DEX, presenting an evaluation the processes and analysis of reaction products, is essential considering the scarcity of PhEC approaches and the numerous studies that indicate DEX as a contaminant in wastewater. In addition to the modifications and improvements in the structural, morphological, and electrochemical properties of $WO_3/BiVO_4$, the analysis of DEX degradation by photolysis and electrocatalysis was also addressed as a way of comparing the processes, in addition to the analysis of products with the identification of short-chain acids and toxicity tests with Lactuca sativa expressing the impact of the PhEC process for environmental applications.

## 2. Materials and methods

### 2.1. Chemicals and materials

One-side conductive glass covered with fluorine-doped tin oxide (FTO) obtained from Sigma-Aldrich (surface resistivity ~7 Ω/sq, 2.2 mm thickness) served as a substrate. All the chemicals, including sodium tungstate ($Na_2WO_4{\cdot}2H_2O$, ≥99 %, Sigma-Aldrich), hydrochloric acid (HCl, 37 %), ammonium oxalate ($(NH_4)_2C_2O_4$, ≥99 %, Sigma-Aldrich), hydrogen peroxide (≥35 %, Sigma-Aldrich), bismuth (III) nitrate pentahydrate ($Bi(NO_3)_3 \cdot 5H_2O$, ≥98 %, Sigma-Aldrich), ammonium metavanadate ($NH_4VO_3$, ≥99.5 %, Reidel-de Haën), polyethylene glycol (PEG300) and Dexamethasone ($C_{22}H_{29}FO_5$, CAS number: 50–02–2, Sigma-Aldrich). Ethanol, acetone, and isopropanol were obtained from Dynamic. All reagents were analytical grade and were used as raw materials without further purification. Carboxylic acid standards were purchased from Sigma Aldrich. All aqueous solutions were prepared with water purified from a Millipore Milli-Q system (> 18.2 MΩ).

### 2.2. Chemical bath deposition and spin coating techniques for $WO_3/BiVO_4$ synthesis

The materials were deposited on an FTO substrate cut into 1 × 1.5 cm slides and washed under ultrasound with soapy water, ethanol, acetone, and isopropanol. Before deposition, a surface treatment was carried out of the FTO with plasma $N_2$ for 5 s in plasma cleaner equipment (Zhengzhou CY-P2L-B) to improve the adhesion of the deposited film. In the first step of the synthesis process, a layer of $WO_3$ film was deposited by reduction of peroxotungstate, based on the method of Cheng et al. [26]. Briefly, a mixture of 1.21 mmol of sodium tungstate, 1.20 mmol of ammonium oxalate, and 33 mL of water was added to a temperature-controlled jacketed glass reactor. Soon after, 9 mL of concentrated HCl, 8 mL of hydrogen peroxide (≥35 %), and 30 mL of ethanol were added dropwise under vigorous stirring, respectively. Finally, the FTO substrate was added to the solution, forming an angle of 45° with the reactor wall. The bath temperature was adjusted to 85 °C for 3 h for the complete precipitation of $WO_3.H_2O$ and the formation of a yellow film under the FTO. After cooling the system to room temperature, the $WO_3.H_2O$ film was washed with water and dried overnight in an oven at 80 °C and subsequently calcined at 500 °C for 30 min in a microwave oven with a ramp of 2 °C $min^{-2}$ to obtain the $WO_3$ film.

After obtaining the $WO_3$ film, a $BiVO_4$ layer was deposited by spin coating. Two precursor solutions (1 and 2) were used in this step. Solution 1 was prepared from the dissolution of 2.14 mmol of $Bi(NO_3)_3{\cdot}5H_2O$ in 5 mL of PEG 300, and solution 2 from 2.14 mmol of $NH_4VO_3$ dissolved in 5 mL of PEG300. An ultrasonic bath was used to aid in the dissolution process. Soon after, these solutions were mixed by pouring solution 1 over solution 2, and with the aid of the ultrasonic bath for 30 min, a homogeneous mixture of dark orange color was obtained. From the final mix, the $BiVO_4$ film was deposited with a spin-coating, adding 40 μL $cm^{-2}$ under the previously obtained $WO_3$ film and applying a speed of 2000 rpm for 30 s. The added layer was pre-dried with hot air for 15 min in an oven, and the final film composed of $WO_3/BiVO_4$ was calcined at 500 °C for 30 min in a microwave oven with a ramp of 2 °C $min^{-2}$. A yellow-green film of $WO_3/BiVO_4$ was obtained at the end of all steps. The same procedure was applied to get a pure $BiVO_4$ film.

### 2.3. Material characterization

The physical characterizations were performed by X-ray diffraction (XRD, XRD-diffractometer XRD-6000, Shimadzu®, Cu kα irradiation, $\lambda = 1.54$ Å, continuous scan, step 0.02°, scan rate 0.5° $min^{-1}$), Raman microspectroscopy with an exposure time of 30 s and an accumulation of 100 spectra in the region of 150–1000 $cm^{-1}$ (633 nm He-Cd laser, 50 mW, coupled to an Olympus BX41 microscope and CCD detector, Horiba

HR 550 spectrometer), and X-ray photoelectron spectroscopy (XPS) (Scientia Omicron ESCA®, Germany) using a monochromatic Al-Kα X-ray source (1486.7 eV). The morphology characterizations were assessed using high-resolution field emission scanning electron microscopy (FE-SEM, Zeiss Supra 35 at 5 kV). The band gap of the prepared photoelectrodes was estimated using the Kubelka-Munk function approach based on the diffuse reflectance spectra measurement [27]. The diffuse reflectance spectroscopy using a UV–Vis-NIR spectrophotometer coupled with an integrating sphere (DRS, Cary 5 G, Varian®).

### *2.4. Electrochemical and photoelectrochemical evaluation*

The photoelectrochemical characterizations were carried out in a three-electrode cell with the photoanodes ($WO_3$, $BiVO_4$, and $WO_3/BiVO_4$), Pt foil, and Ag/AgCl as the working, counter, and reference electrodes, respectively. The electrochemical measurements were carried out using a potentiostat/galvanostat (PGSTAT 302 N, Autolab, Methrom®), and a solar simulator (irradiance 100 $cm^2$) was used as a light source. The films were characterized by linear sweep voltammetry (LSV) in a potential range from 0 to 1.7 V vs. Ag/AgCl with a scan rate of 5 mV $s^{-1}$ and the transient photocurrent at a polarization potential of 1.4 V vs Ag/AgCl in aqueous solutions containing 0.5 mol $L^{-1}$ $Na_2SO_4$ (pH = 6.5) as supporting electrolyte. Applied bias photon to current conversion efficiency (ABPE) was calculated using the following Eq. (1):

$$ABPE\ (\%) = \frac{(J\ x\ (1.23 - V_b)}{P_{light})\ x\ 100\%} \tag{1}$$

Where $J$ refers to the photocurrent density (mA $cm^{-2}$), $V_b$ is the applied bias vs RHE (V), and $P_{light}$ is 100 mW $cm^{-2}$. Electrochemical impedance spectroscopy (EIS) measurements were carried out in 0.5 mol $L^{-1}$ $Na_2SO_4$ (pH = 6.5) both in the dark and under illumination with frequencies ranging from 10 kHz to 0.1 Hz with an AC amplitude of 10 mV and a DC voltage of 1.4 V. To obtain the Mott–Schottky (MS) plot, EIS measurements were carried out in the dark for the photoanodes at a potential range of 0 to 1.8 V vs. Ag/AgCl, optimized frequency of 1 KHz with an AC amplitude of 10 mV using 0.5 mol $L^{-1}$ $Na_2SO_4$ (pH = 6.5) as supporting electrolyte. The films' charge space capacitances (Csc) were obtained, and the MS graph was built by plotting $C_{sc}^{-2}$ vs. the applied potential range. The potential reference values were converted:

$$E\ (vs.\ RHE) = E\ (Ag\,/\,AgCl_{KClsat})\ +\ 0.197\ + 0.059\ x\ pH \tag{2}$$

### *2.5. Photoelectrochemical DEX removal evaluation*

The degradation processes were performed in the same system applied in the photoelectrochemical characterizations, 0.5 mol $L^{-1}$ $Na_2SO_4$ as electrolyte and contaminated with 10 mg $L^{-1}$ DEX, and a volume of 70 mL was treated. For EC and PhEC, 1 mA $cm^{-2}$ of current density was applied, and for photolysis and PhEC, the system was irradiated by a solar simulator (irradiance 100 mW $cm^{-2}$). The evolution of DEX concentration was monitored by HPLC-UV/DAD (Shimadzu Prominence model LC-20AT) using a Luna C18 column (Phenomenex®: 250 mm × 4.6 mm, five µm particle size) as the mobile phase consisting of methanol: water (60:40). The mineralization of the compound was monitored using the Shimadzu TOC-VCPN analyzer. The determination of carbon organic total (TOC) was carried out by determining the inorganic carbon (IC) and total carbon (TC), respectively. The difference in IC obtained the TOC and TC measured values in generated $CO_2$ [28].

Intermediates of reaction degradation short-chain carboxylic acids were also determined throughout the photolysis, EC, and PhEC degradation processes by HPLC. In this case, a Rezek ROA-H™ column from Phenomenex® as the stationary phase and 2.5 mM $H_2SO_4$ as the mobile phase were used at 0.5 mL $min^{-1}$. The carboxylic acids (detected at 210 nm) were identified by comparing their retention times with those of previously analyzed standards. The injection volume and column temperature were maintained at 25 µL and 23 °C, respectively. The effect of oxidizing species on the photoelectrochemical degradation of DEX was evaluated employing PhEC tests with the addition of the following materials (5 mmol $L-1$): isopropanol (ISO), ammonium oxalate (AO), ascorbic acid (AA), and silver nitrate ($AgNO_3$) for $^\bullet OH$, $h^+$, $^\bullet O_2^-$ and $e^-$, respectively.

### *2.6. Performance parameters*

The synergistic coefficient (%) was calculated using Eq. (3) [29], where k is the kinetic constant calculated for the different single and combined processes studied (photolysis, EC, and PhEC).

$$Sinergy\ coefficient\ (\%)\ = \frac{K_{Photoelectro}\ -\ K_{Electro}\ -\ K_{Photolysis}}{K_{Photolysis}\ +\ K_{Electro}}\ x\ 100 \tag{3}$$

The energy consumption per degraded mass rate of DEX ($EC_{DEX}$ (kWh mg $L^{-1}$)) was calculated for the photolysis, electrocatalysis, and PhEC processes applied using Eq. (4) below:

$$EC_{DEX}\ \left(kWh\ mg\ L^{-1}\right) = \frac{E_{cell}\ x\ Ix\ t + P\ x\ t}{V_s\ x\ k_{DEX}} \tag{4}$$

Where $E_{cell}$ is the average cell potential (V), $I$ is the applied current (A), $t$ is the electrolysis time (h), P is the nominal power of the lamp (W), $V_s$ is the solution volume (L), and $k_{DEX}$ is the DEX removal rate (mg $L^{-1}$).

### *2.7. Phytotoxicological studies*

To evaluate the efficiency of the PhEC process, the level of toxicity of the degradation products was analyzed in comparison with the parent compound (DEX) using a phytotoxicity study. The phytotoxicity test was carried out using lettuce seeds (*Lactuca sativa*), a method previously described by Assis et al. (. (Assis et al. 2022). In the test, 20 surface-sterilized seeds were placed in a Petri dish lined with filter paper where 4 ml of the test solution (DEX or its degraded products) or deionized water (control) was added. The plates containing the seeds were then placed in an environment with temperature and humidity control in the dark for 120 h. In the end, the level of toxicity was analyzed in terms of inhibition of seed germination and germination length compared to the control, with the distilled water having 100 % germination for the seeds and the maximum germination length. The tests were performed in triplicate.

## 3. Results and discussions

### *3.1. Characterization of photoelectrocatalytic films*

The morphological properties, and the average grain size of the photoelectrodes were observed and evaluated using field-emission scanning electron microscopy (FE-SEM). Fig. 1(a) shows the micrographic images of the morphology of the $WO_3$ photoanode. It is observed that the application of the chemical bath method from the peroxotungstate route and calcination at 500 °C in a microwave oven induced the formation of nanoflakes (petals) connected forming 3D nanoflowers by self-assembly with a smooth surface and an average diameter of 0.816 ± 0.257 µm. From Fig. 1(d), it is possible to observe that the nanoflakes (petals) have a growth perpendicular to the substrate, with this layer having 1.204 ± 8.42 µm. Fig. 1(b) shows the morphology of the $BiVO_4$ film, which exhibits globular particles with an average size of 0.405 ± 0.103 µm. Since only a thin layer of $BiVO_4$ was applied to the substrate, it was impossible to observe a homogeneous layer with high resolution, as shown in Fig. 1(e). Interestingly, the micrography obtained for the $BiVO_4$ deposited on the preformed $WO_3$ film shows a different aspect than both materials. After coating the $WO_3$ film with the $BiVO_4$ layer, the film obtained showed a flake-like morphology with a larger diameter than that of pure $WO_3$ and a rough surface. This indicated the growth of globular particles under the plates and the uniform

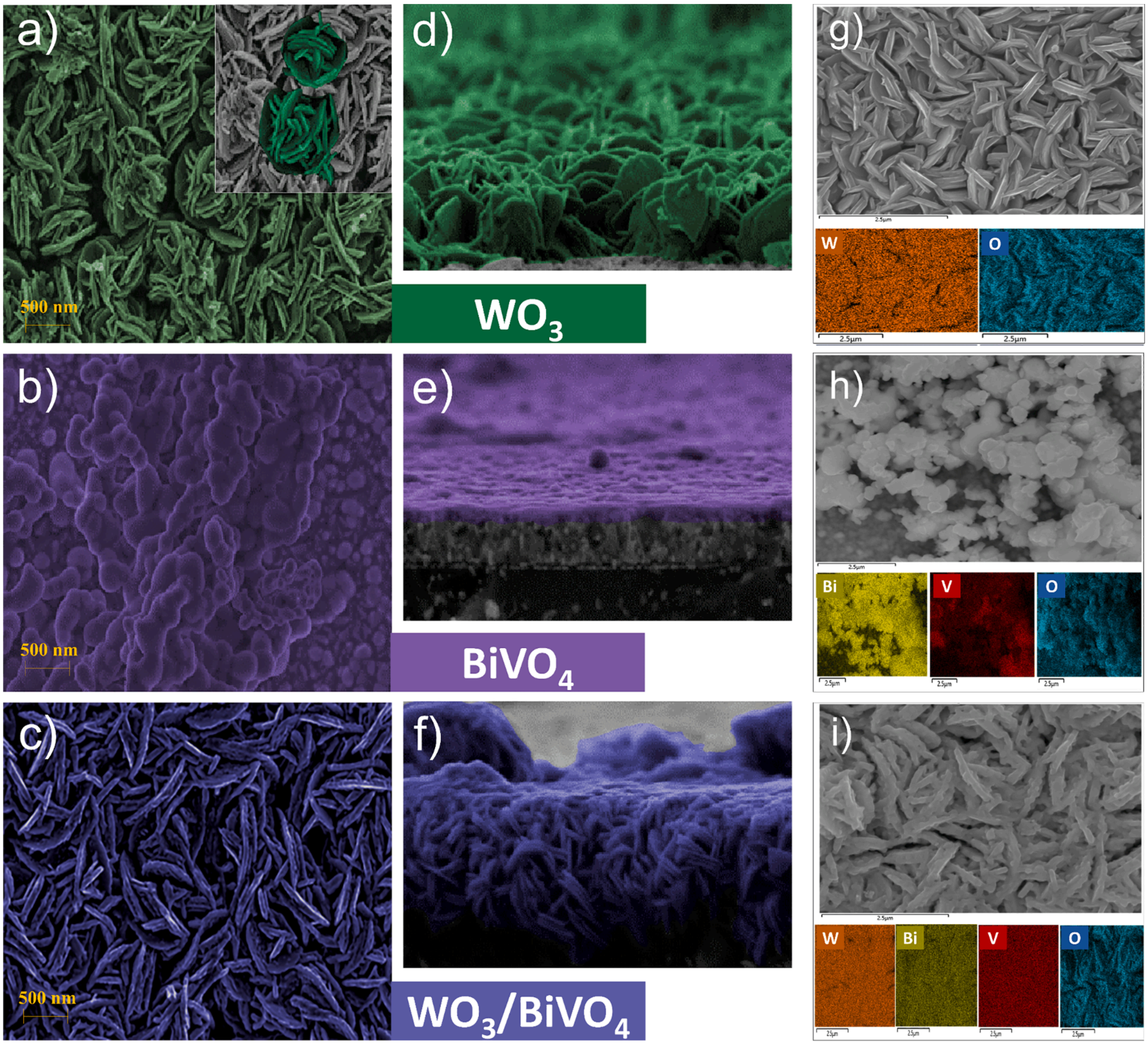

**Fig. 1.** Scanning electron micrographs and cross-section of the (a-d) $WO_3$, (b-e) $BiVO_4$, and (c-f) $WO_3/BiVO_4$ photoanodes. EDS mapping images for the (g) $WO_3$, (h) $BiVO_4$, and (i) $WO_3/BiVO_4$ electrodes.

adhesion of $BiVO_4$ to the $WO_3$ nanoflakes (Fig. 1(c)). The average flake size for the $WO_3/BiVO_4$ structure was 1.050 ± 0.245 μm. As observed in Fig. 1(f), this material presented a thickness of 1.847 ± 1.56 μm, and the flakes composed of $WO_3$ and $BiVO_4$ overlapped, forming a thick layer. The FE-SEM images demonstrate the excellent formation of $WO_3$, $BiVO_4$, and $WO_3/BiVO_4$ films obtained by chemical bath and spin coating methods. The increase in the length of the flake structure from the formation of the heterojunction can enhance light capture by the electrode [31]. EDS mapping presented in Fig. 1 (g-i) confirmed the composition of the films, demonstrating the existence of W and O in the $WO_3$ films, the presence of Bi, V, and O in the $BiVO_4$ films, and the coexistence of W, Bi, V, and O elements well distributed in the synthesized heterojunction film.

Crystallographic analysis of the samples can reveal more details about forming a heterojunction of the proposed oxides. Fig. 2(a) illustrates the diffractograms of the $WO_3$, $BiVO_4$, and $WO_3/BiVO_4$ photoanodes. All the samples showed characteristic peaks associated with the FTO substrate (identified by symbol *) at the values of $2\theta = 26.6°$, 33.75°, 37.86°, 51.5°, 61.74°, and 65.62° The pristine $WO_3$ film showed diffraction peaks at $2\theta$ values of 23.2°, 23.7°, and 24.4°, main peaks characteristic crystallographic planes of a Miller index (002), (020), and (200), which are attributed to the monoclinic phase $WO_3$ (JCPDS No 01–75–2072) [32]. For the $BiVO_4$ film, the diffraction peaks at $2\theta$ values of 18.7, 18.9, and 28.9° can be seen as the peaks of the Miller index (110) e (121), which reveals the attainment of the monoclinic $BiVO_4$ phase (JCPDS No 014–0688) [33]. The XRD of the heterojunction results in the combination of the phases of both oxides. The formation of the $WO_3$ and $BiVO_4$ phases can be observed at the $2\theta$ position, as recorded for each material separately. In addition, an increase in the intensity of the peak located in the region between 28° and 29° is observed, indicating a possible overlap of the (112) planes for the $WO_3$ phase and the (121) plane for the $BiVO_4$ phase can be observed, confirming the formation of the $WO_3/BiVO_4$ heterojunction [22]. Similar observations were suggested by Lima et al. (2022) when studying the formation of heterostructures from $CuWO_4$ and $MnWO_4$, where the changes suffered by the superposition of peaks in the (111) planes for the $CuWO_4$ phase and the (111) and ($\bar{1}11$) planes for the $MnWO_4$ phase were essential for confirming the obtained heterojunction. Furthermore, no additional phases were detected and observed in the diffractograms, indicating the successful obtaining of pure or heterojunction films [34]. Fig. 2(b) shows the illustrative representation of the monoclinic unit cells of $BiVO_4$ and $WO_3$. The $BiVO_4$ phase is a scheelite-type monoclinic, with lattice parameters $a = 5.195$ Å, $b = 11.701$ Å, $c = 5.092$ Å and $\beta = 90.38°$, belonging to the space group ($I2/a$) [35]. For monoclinic $WO_3$, the structure is formed by octahedral clusters of $[WO_6]$, belongs to the symmetry space group ($P21/a$) and has lattice parameters $a = 7.274$ Å, $b = 7.501$ Å and $c = 3.824$ Å, angles $\alpha = \gamma = 90°$ and $\beta = 89.93°$ [36].

Fig. 2(b) presents the Raman analyses of the synthesized films and

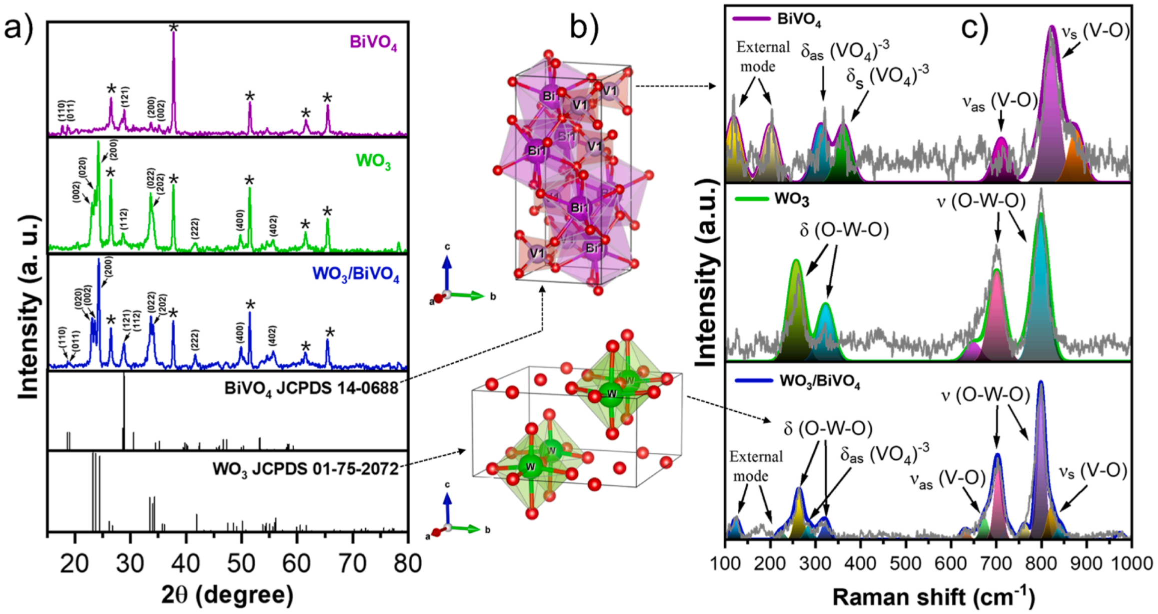

**Fig. 2.** X-ray diffractograms of the (a) WO$_3$, BiVO$_4$, and WO$_3$/BiVO$_4$ electrodes, (b) schematic representation of monoclinic BiVO$_4$ unit cell (ICSD n°. 100,604) and monoclinic WO$_3$ unit cell (ICSD n°. 31,823), and Raman spectra of (c) WO$_3$, BiVO$_4$, and WO$_3$/BiVO$_4$ electrodes.

the spectra's deconvolution. The Raman spectra of pure WO$_3$ in Fig. 2(a) show a set of more intense peaks at 798 cm$^{-1}$ and 701 cm$^{-1}$ attributed to the O–W–O stretching modes [37]. Meanwhile, the 263 cm$^{-1}$ and 320 cm$^{-1}$ peaks can beattributed to the W–O–W bending vibrations of the WO$_3$ monoclinic phase [38]. For BiVO$_4$, peaks at 810 and 713 cm$^{-1}$ corresponding to the symmetric and antisymmetric stretching of the V–O bond are observed. In addition, peaks around 362 and 3112 cm$^{-1}$ were observed, which contemplate the asymmetric and symmetric configurations of the [VO$_4$] tetrahedron, respectively, and peaks at 200.4 and 119.3 cm$^{-1}$ related to the external mode corresponding to the

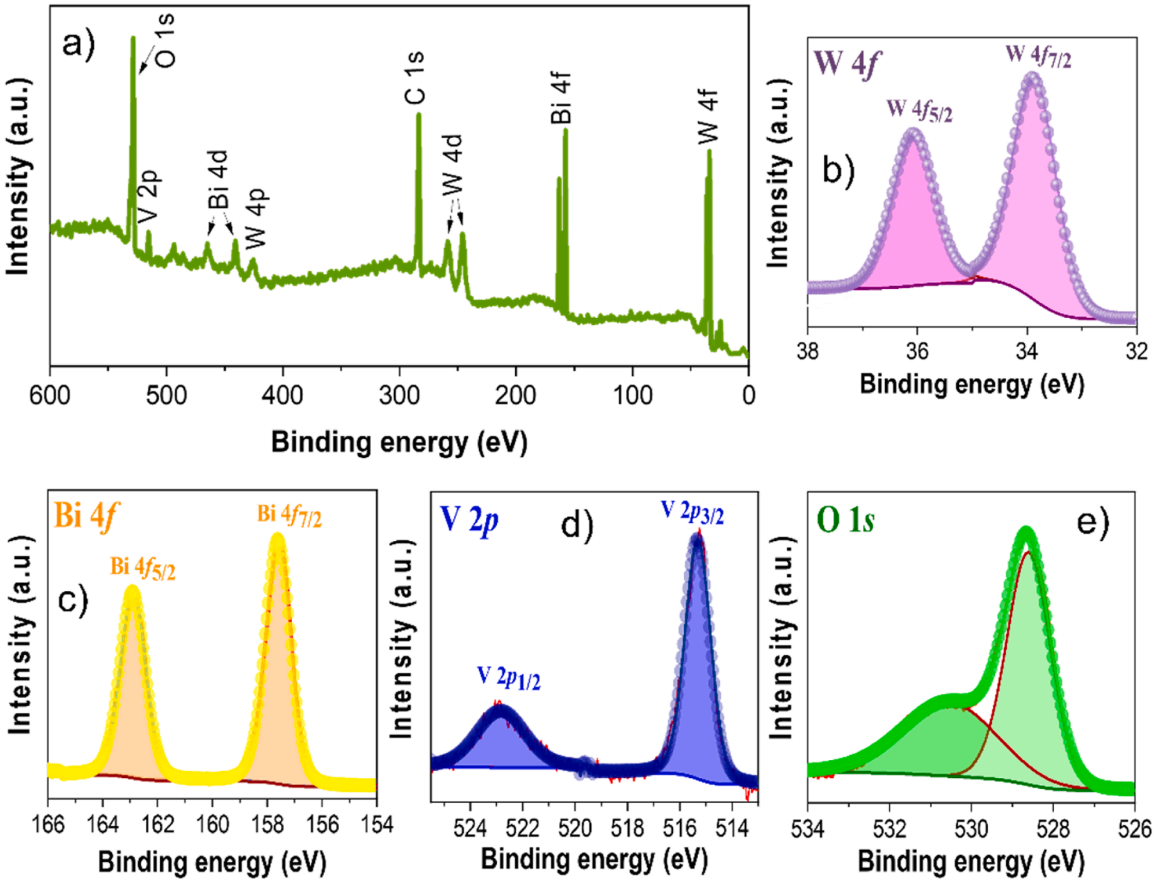

**Fig. 3.** XPS spectra of the WO$_3$/BiVO$_4$ electrode: (a) the survey spectrum, (b) W 4f, (c) Bi 4f, (d) V 2p, and (e) O 1s.

rotation/translation vibration of the crystal structure [27,35]. Finally, the Raman spectra of the $WO_3/BiVO_4$ film show a set of deconvoluted peaks associated with the pure materials and shifts of the set of vibration peaks at 798.5 and 320 $cm^{-1}$ due to a probable distortion of the structure related to the formation of the heterojunction [25]. The existence of shifts occurring in the peak located in the region of 740 to 850 $cm^{-1}$ for the $WO_3/BiVO_4$ film when compared to pristine $WO_3$ and $BiVO_4$ may be an indication of the formation of W-O-V bonds, related to the insertion of W in the V sites of the $BiVO_4$ lattice and the occurrence of the heterojunction between $WO_3$ and $BiVO_4$. The vibrational modes of both materials are observed in the $WO_3/BiVO_4$ heterostructure. Similar behavior for $WO_3/BiVO_4$ structures is shown by Yin et al. (2017) in their studies, demonstrating that the interaction of these two materials and the modifications undergone for the formation of a heterojunction directly influenced the photoelectrochemical behavior and the absorption of visible light [39]. The Raman results obtained for the photoanodes and the obtained heterojunction agree with the XRD results.

XPS analysis revealed the valence states of the elements and surface chemical compositions of the $WO_3/BiVO_4$ heterojunction film. As a surface-sensitive technique, XPS analysis predominantly reveals the composition of the $WO_3/BiVO_4$ film, as summarized in Fig. 3. The survey XPS spectrum (Fig. 3(a)) confirms the presence of tungsten (W), bismuth (Bi), vanadium (V), and oxygen (O) atoms in stable oxidation states ($W^{6+}$, $Bi^{3+}$, $V^{5+}$, and $O^{2-}$) to electronic states in 4f, 4f, 2p and 1s orbitals, respectively. The peaks related to the bond energies W 2p, W 4d, and Bi 4d are observed. The binding energies were calibrated using the C 1s equal to 284.5 eV [40]. The high-resolution W 4f XPS spectrum in Fig. 3(b) shows the presence of two peaks (at 36.1 eV and 33.9 eV) related to the binding energies for W 4f5/2 and W 4f7/2, which corresponds in the oxidation state of $W^{6+}$ ions to tungsten oxide. The peaks of the Bi $4f_{5/2}$ and $4f_{7/2}$ spectra at 162.8 and 157.5 eV (Fig. 3(c)) are related to the surface $Bi^{3+}$ species in the $BiVO_4$ compound. The peaks of V $2p_{3/2}$ and V $2p_{1/2}$ are at around 522.9 and 515.3 eV (Fig. 3(d)), which are reported values for $V^{5+}$ in $BiVO_4$ [41]. The XPS spectra confirmed the formation of the film from the heterojunction of $BiVO_4$ and $WO_3$, corroborating the findings FE-SEM, XRD, and Raman analyses. The binding energy of the O 1s orbitals (Fig. 3(e)) after deconvolution showed two Gaussian peaks; the strong peak at 528.6 eV can be related to the lattice oxygen in metal oxides ($BiVO_4$ and $WO_3$) and surface hydroxide (530.6 eV), which agrees with the reported literature for other oxide material films [17,42]. Thus, the $WO_3/BiVO_4$ film composition was characterized morphologically and structurally, demonstrating the coexistence of the materials in the photoelectrode.

### *3.2. Visible light harvests performance photoelectrocatalytic films*

The production of photoanodes and their modifications aim to leverage the light-harvesting response of semiconductors and improve electrochemical properties under light excitation. To investigate the optical properties of $WO_3$, $BiVO_4$, and $WO_3/BiVO_4$ films, the energy

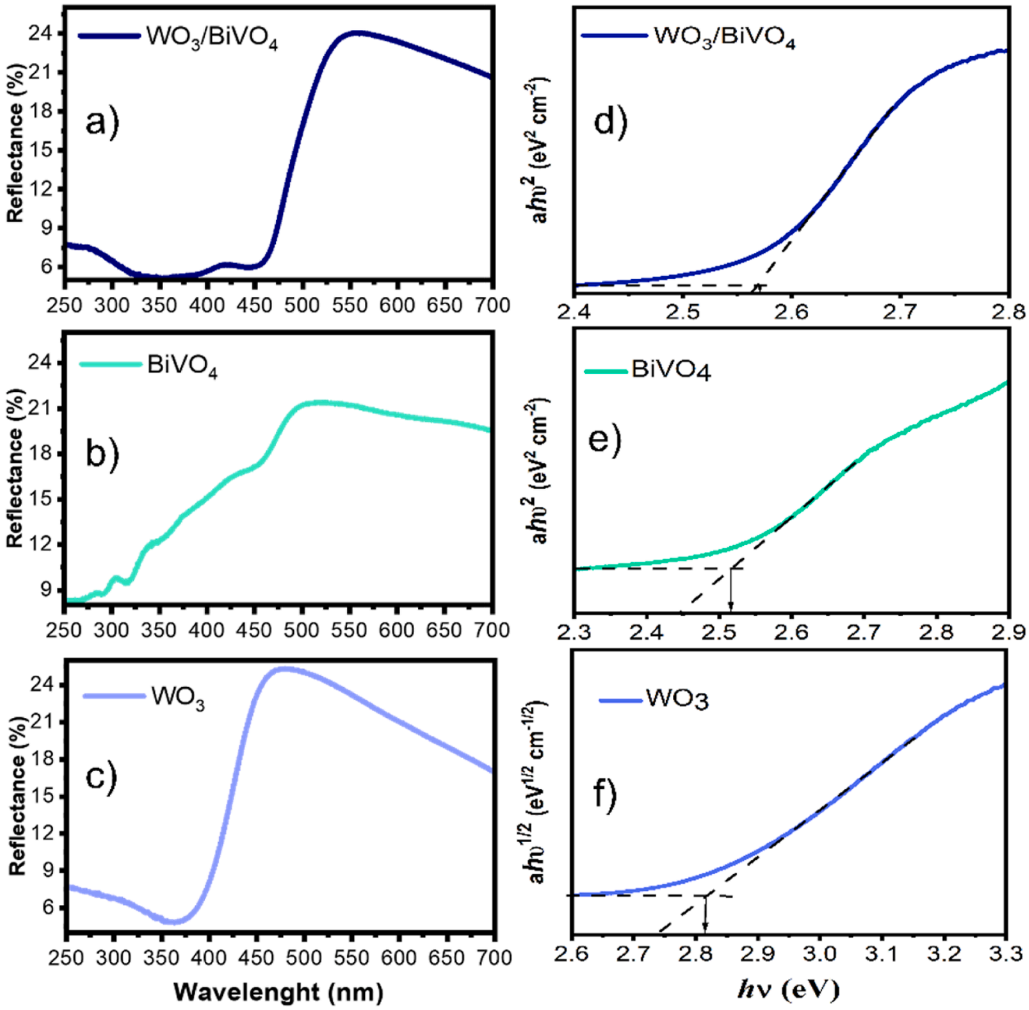

**Fig. 4.** UV−vis diffuse reflectance spectra of (a) $WO_3$, (b) $BiVO_4$, and (c) $WO_3/BiVO_4$ electrodes. Optical band from Tauc plot gap energy ($E_g$) of the (d) $WO_3$, (e) $BiVO_4$, and (f) $WO_3/BiVO_4$ electrodes.

band structures of these pure materials and the obtained heterojunction were studied by UV–Vis DRS. The UV–vis DRS spectra observed in Fig. 4 (a-c) show, by the decay of the reflectance value, that the light absorption in the films remains throughout the visible spectrum region (from 700 nm to ~400 nm) [43]. As observed, the absorption edge of the $WO_3$ film is located at ca. 450 nm; for the $BiVO_4$ film, it extends to ca. 490 nm. The $WO_3/BiVO_4$ heterojunction has an absorption edge of around 485 nm, exhibiting properties like the $BiVO_4$ film [23]. The band gap was determined using the Kubelka-Munk function. The band gap energy values ($E_g$) were calculated using the following equations [27]:

$$\alpha = F(R) = (1-R)^2/2R \text{ and } (\alpha h\nu)^2 = A\left(h\nu - E_g\right) \tag{5}$$

Where α is the absorption coefficient, F(R) is the Kubelka-Munk function, R is the absolute reflectance for a given hν, h is Planck's constant, ν is the frequency of light, and A is a constant. The variable n is a parameter that depends on the interband transition, assuming 2 or 2/3 for direct transitions (allowed and forbidden, respectively) and 1/2 or 1/3 for indirect transitions (allowed and forbidden, respectively). Then, for the absorption spectra, a sharp linear increase is characteristic for each material, and when crossed with the x-axis, an approximation of the band gap is provided [44].

Fig. 4(d) shows that the pure $WO_3$ film presented a band gap value of 2.8 eV, which agrees with the theoretical values presented in other studies [45,46]. The absorption spectra for $BiVO_4$ (Fig. 4(e)) shows a band gap value of 2.52 eV, which agrees with previously reported values [24,26]. The $WO_3/BiVO_4$ heterojunction (Fig. 4(f)) presented an $E_g$ value of 2.56 eV, which is very close to that obtained for the pure $BiVO_4$ film. This relationship can be explained by the thickness and capture of

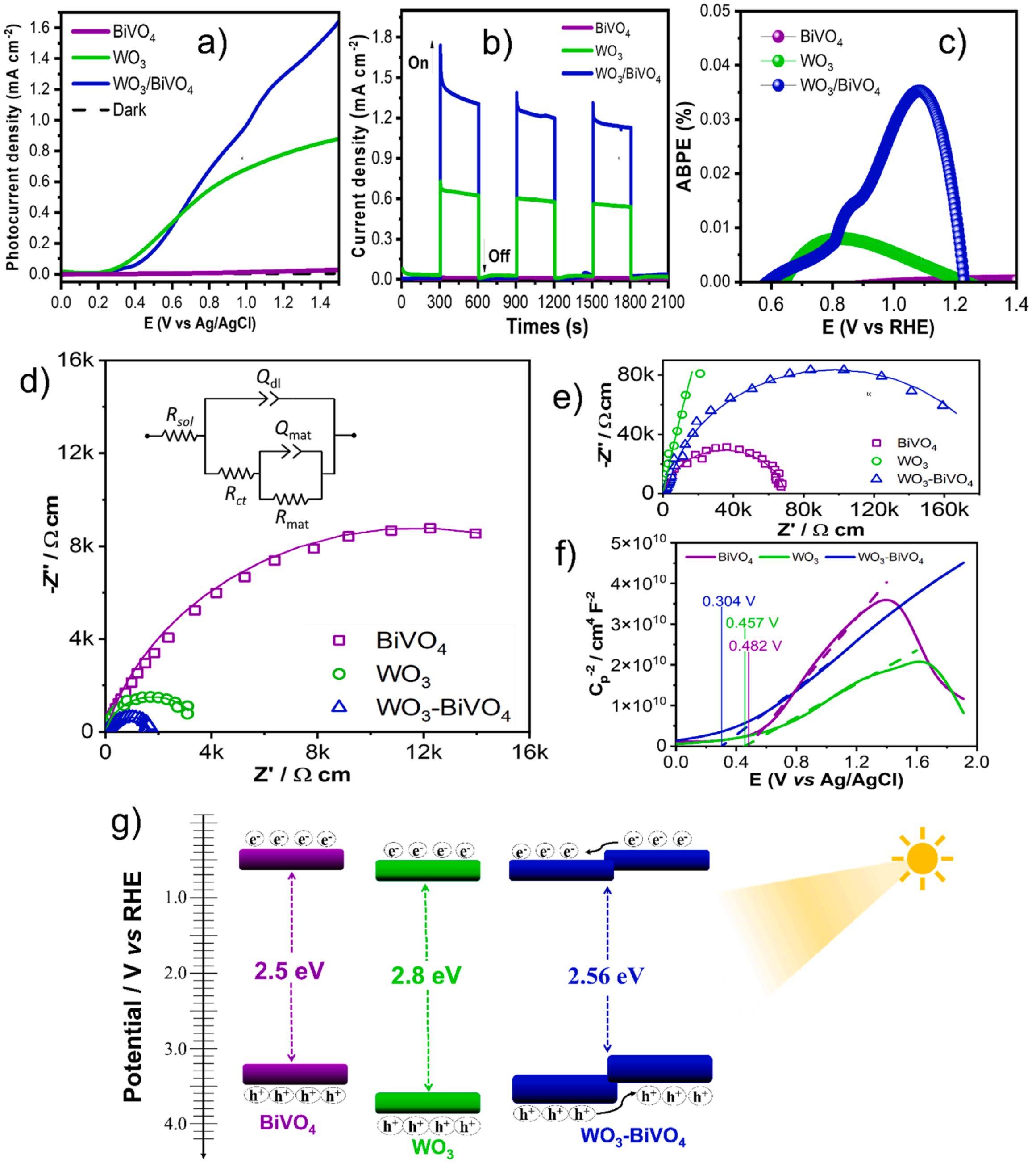

**Fig. 5.** (a) Linear sweep voltammetry curves under chopped light illumination, (b) Transient photocurrent curve (300 s interval) at 1.4 V vs. Ag/AgCl, (c) ABPE efficiency, (d) Nyquist plots at 1.4 V vs. Ag/AgCl under illumination, (e) Nyquist plots at 1.4 V vs. Ag/AgCl without illumination, (f) Mott-Schottky plots registered in 0.5 mol $L^{-1}$ $Na_2SO_4$ at 5 mV $s^{-1}$, and (g) Diagram of the band edge position for the $WO_3$, $BiVO_4$ and $WO_3/BiVO_4$ electrodes.

the band gap energy of the surface layer of the film after the addition of $BiVO_4$ to the $WO_3$ surface [47]. The band gap evaluation illustrates the visible light capture of the $WO_3/BiVO_4$ heterojunction and an assessment of the photoactivity of the obtained material. Therefore, irradiation with light at 485 nm can exceed the band gap energy required to promote an electron from the valence band to the conduction band. Furthermore, the electrochemical behavior of each material needs to be evaluated to determine the conditions for an ideal photoelectrochemical response.

### *3.3. Electrochemical characterization of photoelectrocatalytic films*

The films obtained photoelectrochemical properties were analyzed using a three-electrode system in a 0.5 mol $L^{-1}$ $Na_2SO_4$ aqueous solution (pH 6.5), with $WO_3$, $BiVO_4$, and $WO_3/BiVO_4$ electrodes as the WE, Pt as the counter electrode, and Ag/AgCl as the reference. Fig. 5(a) illustrates the LSV and the comparative current response of the three materials under irradiation, as well as a blank measurement under dark conditions. The LSV measurements showed that all electrodes presented positive photocurrent values as the potential increased, as expected for n-type semiconductors such as $WO_3$ and $BiVO_4$ at positive potentials. In this condition, the process of separation of the photogenerated charge carriers occurs, the $h^+$ moves to the electrode surface, oxidizing the species in the solution, and the $e^-$ is conducted to the external circuit, producing anodic photocurrent [48]. It can be observed that the current response of the films under dark conditions is small when compared to the photoelectrocatalytic response recorded under visible irradiation. The comparative LSV shows that $WO_3$ (0.9 mA $cm^{-2}$) presents an order of magnitude higher current response than pure $BiVO_4$ (0.03 mA $cm^{-2}$). This behavior has been previously described and justified by the greater separation of charge carriers in the $WO_3$ film that stabilizes the photogenerated species compared to $BiVO_4$ [37,49]. Meanwhile, the $WO_3/BiVO_4$ heterojunction presents a photocurrent density (1.6 mA $cm^{-2}$) of magnitude 1.8 and 53 times higher than $WO_3$ and pure $BiVO_4$ [49]. This behavior was associated with the better separation of charge carriers across the interface of the combined semiconductors. The $WO_3/BiVO_4$ heterojunction extends the lifetime of charge carriers and improves the current response and the ability to generate oxidizing species. The transient photocurrent measurements described in Fig. 5(b) illustrate the long-term stability response of $WO_3/BiVO_4$ compared to the pure electrodes. As can be seen, an initial anodic photocurrent peak forms due to the injection of electrons into the external circuit, caused by charge separation immediately after the film irradiation process, i.e., the formation of $e^-/h^+$ pairs. Upon stopping the irradiation, the electron in the semiconductor conduction band returns to the VB, resulting in a null photocurrent. This behavior demonstrates that the sensitive response of the film to light is expressed by the processes described above without the influence of additional reactions in the electrochemical system. The transient current results agree with the values observed in the LSV. The ABPE was applied to express the efficiency of using incident light in photoelectrochemical conversion by photoelectrodes. The ABPE shown in Fig. 5(c) was calculated from the LSV curves. As can be seen, $BiVO_4$ showed a maximum value of ABPE at 1.1 $V_{RHE}$ with 0.002 %. On the other hand, the $WO_3$ film presented an ABPE value of 0.005 % at 1.0 VRHE, and a higher ABPE was obtained for the $WO_3/BiVO_4$ film of 0.035 %.

The electrochemical impedance curves of the $WO_3$, $BiVO_4$, and $WO_3/BiVO_4$ photoanodes were obtained under light irradiation (Fig. 5(d)) to investigate the kinetics of charge transfer behavior at the electrode-electrolyte interface [50]. Using the information from the impedance spectra obtained under illumination, it is possible to estimate essential parameters in photoanodes, such as the times and lifetimes of electron-hole pairs and their mobility, which indicate the efficiency of the material in converting light energy. Fig. 5(e) shows the Nyquist plots for the electrodes without illumination, which are consistent with the characteristics of the materials. $WO_3$ is a metallic oxide with more insulating characteristics than $BiVO_4$; however, the composite obtained from both shows a significant improvement in this characteristic, although it still has more excellent resistance than pure $BiVO_4$. It is important to note that factors influencing the electronic structure of materials can cause significant changes in the obtained values. Therefore, it was concluded that the formation of the $BiVO_4/WO_3$ composite altered its electronic structure, impacting both the experimentally determined bandgap and flat band potential, resulting in new values.

Furthermore, it is necessary to adjust the impedance data to obtain accurate information about the characterized materials. Fig. 5(d) inset shows the model used, which is widely applied in composite materials [51,52]. The solution resistance ($R_{sol}$) describes the conductivity of the electrolyte; in series, there are the charge transfer resistance ($R_{ct}$) and the electrical double layer pseudocapacitance ($Q_{dl}$), both used to accurately describe the electrode-electrolyte interface and kinetics of the electrochemical reactions. In series with the $R_{ct}$, there are both the resistance and the pseudocapacitance of the material ($R_{mat}$ and $Q_{mat}$), which describe both the conductivity of the material and the delay in electrical conduction due to the motion of charge carriers. Thus, Table 1 brings together all the parameters and characteristics of the materials.

Analyzing the Nyquist graph, Fig. 5(d), it is possible to notice that the larger the photocurrent, the smaller the observed semicircle. This occurs because the photogenerated current is felt to be a decrease in the total impedance of the system. After all, with the same AC disturbance, more current is generated. Consequently, charge transfer parameters are also affected, i.e., the resistance to charge transfer drops while the charge transfer rate increases. On the other hand, it is interesting that pure $WO_3$ without illumination shows a high resistivity, which is discussed in several references [53,54]. The effect of the heterojunction shows an essential drop in the general resistance, suggesting a significant synergistic effect. Finally, Fig. 5(f) shows the Mott-Schottky plot for the samples, where it is possible to see that the mixture shows a shift in the flat-band ($E_{fb}$) potential to lower potential compared to the pure samples that have very close $E_{fb}$ values. Once the $E_{fb}$ is related to the band edges of a semiconductor, and in the case of an n-type, to the valence band, this value is significant to address the excellent performance of photocatalytic materials [55,56].

Table 1 summarizes parameters found using electrochemical impedance spectroscopy and the Mott-Schottky plot [52]. The values of $\chi^2$ demonstrated the excellent fitting of the data using the proposed model. Besides, the values of charge-transfer resistance under illumination agree with the performance observed for the samples. However, the significant improvement observed from the electronic structure point of view is related to both; the shift of $E_{fb}$ to a lower potential aligns with an increase in the amount of charge carriers in the heterojunction, which increases 3.3 and 25.9 times when compared to $WO_3$ and $BiVO_4$, respectively. These modifications were fundamental for the rapid degradation of DEX. Therefore, the function of each material can be summarized by considering that $WO_3$ acts as a scaffolding material for the growth of $BiVO_4$ grains, which drastically modifies the obtained heterojunction morphology. The formation of the $WO_3/BiVO_4$ heterojunction serves as a photoactive surface light collector, exhibiting low charge transfer resistances, which indicates a well-executed heterojunction with excited electrons available for charge transfer processes. So, with more charge carriers, more charge can be transferred to the molecule to degrade it. From the parameters obtained and presented in Table 1, band diagrams were constructed for the pure materials and the heterojunction $WO_3/BiVO_4$ (Fig. 5(g)).

### *3.4. Photoelectrocatalytic degradation of DEX under different operational modes*

Fig. 6 shows the results of DEX degradation in a synthetic residue containing 10 mg $L^{-1}$ of the anti-inflammatory and 0.5 mol $L^{-1}$ $Na_2SO_4$ for 120 min using the $WO_3/BiVO_4$ electrode. To identify the contribution of photochemical and electrochemical activities, the $WO_3/BiVO_4$

**Table 1**
Impedance spectroscopy, Mott-Schottky and Kubelka-Munk parameters.

| | **$BiVO_4$** | | **$WO_3$** | | **$WO_3/BiVO_4$** | |
|---|---|---|---|---|---|---|
| | ***dark*** | ***light*** | ***dark*** | ***light*** | dark | light |
| $R_{ct}$ / kΩ $cm^2$ | 14.9 | 1.781 | 26.9 | 0.142 | 7.54 | 0.0232 |
| $R_{mat}$ / kΩ $cm^2$ | 54.8 | 23.7 | 5.38 | 3.55 | 1.86 | 2.05 |
| $Q_{dl}$ / μF $s^{n-1}$ $cm^{-2}$ | 4.43 | 5.589 | 40.9 | 0.125 | 10.4 | 2.42 |
| $n_{dl}$ | 0.880 | 0.801 | 0.893 | 0.719 | 0.884 | 1.00 |
| $Q_{mat}$ / μF $s^{n-1}$ $cm^{-2}$ | 0.548 | 0.502 | 0.283 | 59.7 | 13.0 | 50.9 |
| not | 1.00 | 1.00 | 0.646 | 0.899 | 0.945 | 0.640 |
| $\chi^2$ | $2.18\times10^{-4}$ | $3.14\times10^{-4}$ | $6.73\times10^{-4}$ | $4.43\times10^{-4}$ | $6.18\times10^{-4}$ | $2.72\times10^{-4}$ |
| $N_D$ / $\times10^{17}$ $cm^3$ | 5.75 | | 45.4 | | 149 | |
| $E_{fb}$ / V vs. Ag/AgCl/$KCl_{sat}$ | 0.482 | | 0.457 | | 0.304 | |
| $E_g$ / eV | 2.502 | | 2.804 | | 2.560 | |

film was evaluated under different treatment conditions for dexamethasone removal: photolysis, EC, and PhEC, as illustrated in Fig. 6(a).

The electrocatalysis with the application of 1 mA $cm^{-2}$ promoted a prolonged degradation of DEX with only 13 % after 120 min, demonstrating that the electrochemical process alone could not promote the generation of reactive oxygen species with high oxidizing power for efficient removal of the anti-inflammatory. Meanwhile, in the photolysis test under irradiation conditions and without the application of current density, the degradation rate was much higher, showing a removal of 76 %. This result indicates that several reaction processes can occur in the presence of light in a sulfate medium. Initially, degradation can occur by direct photolysis from the absorption of UV light radiation (250–300 nm) present in the irradiation source applied by functional groups and heteroatoms of the molecule, or indirect photolysis with the degradation of photosensitizing species, Eq (6) go [57]. According to Quaresma et al. (2021), when performing the photolysis of DEX, the formation of DEX-375 can occur, which is the main product resulting from this process and is related to the dehydration of the initial molecule [58]

$$DEX + h\nu \rightarrow products \quad (6)$$

The photoelectrocatalytic treatment illustrates the synergistic contribution of the combination of light with the application of 1 mA $cm^{-2}$ in removing DEX, reaching 100 % degradation of DEX at the end of 120 min. The superior performance for PhEC may be related to the improved formation and stabilization of reactive oxygen species on the photoanode surface, using more efficient light irradiation and the applied photocurrent density compared to the individual conditions, providing greater DEX oxidation and efficient degradation. In addition, it reduces the recombination process of the photogenerated $e^-/h^+$ pairs, corroborating the results previously obtained in the electrochemical characterization of the material. The kinetic order of DEX degradation was determined for photolysis, EC, and PhEC (Fig. 6(b)). The kinetics of DEX removal was assessed considering the pseudo-first-order ($\ln (C_t/C_0) = -kt$), where k is the reaction rate kinetic constant, $C_0$ is the initial concentration of DEX and $C_t$ is the concentration of DEX at each time t (min). The rate constants were expressed from the linear extrapolations presented in Fig. 6(b). The degradation rate constants obtained for photolysis and electrocatalysis were 0.0126 $min^{-1}$ ($r^2 = 0.999$) and 0.0010 $min^{-1}$ ($r^2 = 0.986$), respectively. However, for PhEC, a value of 0.0650 $min^{-1}$ ($r^2 = 0.975$) was obtained; as observed, the value obtained for the rate constant of photoelectrocatalysis was higher than in the photolysis and electrocatalysis experiments, approximately 5.2x and 65x, respectively. This result highlights the synergistic effect between light and current density applied to the $WO_3/BiVO_4$ electrode. Applying Eq. (3), the synergistic effect of coupling visible light irradiation to the electrode with the application of a current density of 1 mA $cm^{-2}$ was expressed, obtaining a value of 377.94 %. The value obtained for the synergistic effect proves the efficiency of photoelectrocatalytic technology compared to photolysis and electrocatalysis in the degradation of the anti-inflammatory DEX; similar results were found by Santos et al. (2020) [59].

Fig. 6(c) shows the degree of DEX mineralization after 120 min of reaction under different treatment conditions. It can be observed that photoelectrochemical degradation removed more organic matter (30 %) than photolysis (16 %) and electrocatalysis (1 %). Furthermore, energy consumption was expressed by the mass values of DEX removed. As observed, the photoelectrocatalytic experiment applying 1 mA $cm^{-2}$ requires less energy to promote the removal of a more significant amount of organic matter. These results demonstrate the inefficiency of photolysis and electrocatalysis separately and the excellent performance of PhEC, as shown previously. The PhEC removal efficiency at 1.0 mA $cm^{-2}$ was verified by comparing the DEX removal values at 0.5 and 2.0 mA $cm^{-2}$, described in Fig. 6(d). At 1.0 mA $cm^{-2}$, the DEX removal was 100 %, while at 0.5 and 2.0 mA $cm^{-2}$, the removal dropped to 93 and 90 %, respectively. Therefore, applying current densities of 0.5 and 2.0 mA $cm^{-2}$, it is not possible to obtain a total DEX removal, demonstrating that at 0.5 mA $cm^{-2}$, the reaction is not conducted efficiently and by increasing the current density to 2.0 mA $cm^{-2}$, side reactions such as the oxygen evolution reaction (OER) can limit the removal efficiency at this condition. Similar results were described by Gonzaga et al. (2024) [60].

Additionally, to better understand the degradation of DEX, an analysis of short-chain carboxylic acids was performed, and the formation of four different acids was observed: oxalic, succinic, glycolic, and adipic (Fig. 6(e)). Photolysis was observed to form only one acid, oxalic, and in low concentration (0.12 mg $L^{-1}$). On the other hand, the EC and PhEC processes form all the acids found in concentrations ranging from 2 to 45 mg $L^{-1}$. The formation of carboxylic acids probably did not occur in photolysis because there was no effective degradation of the molecule, as previously suggested. Despite the low removal rate of electrocatalysis, the formation of carboxylic acids was observed. The formation of more significant amounts of carboxylic acids for PhEC agrees with the high degradation rate of DEX and the mineralization of only 30 % of organic matter. Recent studies have shown that transforming organic compounds into short-chain carboxylic acids can reduce the toxicity of effluents [61,62]. Fig. 6(f) focuses on reusing the $WO_3/BiVO_4$ photoelectrode in the PhEC degradation of DEX for five cycles applying 1 mA $cm^{-2}$. As shown, the high DEX removal is maintained with a reduction of only 20 % from the fourth to the fifth degradation cycle. This result demonstrates the high reusability and stability of the electrode with satisfaction.

Based on the above, the good morphological, structural, optical, and electrochemical properties obtained after the formation of the $WO_3/BiVO_4$ heterojunction under the conditions and methods applied were fundamental for the excellent performance of the proposed material in the degradation of the anti-inflammatory DEX. Therefore, these results demonstrate the effectiveness of the photoelectrocatalytic process using the $WO_3/BiVO_4$ anode for environmentally relevant concentrations of DEX with competitiveness to heterojunction electrodes reported in the literature, see Table S1. As previously reported, the quality and stability of the electrode are essential factors for applying photoanodes in PhEC. To evaluate the electrode quality after the photoelectrolysis process cycles during the 120 min reaction, a used $WO_3/BiVO_4$ film was

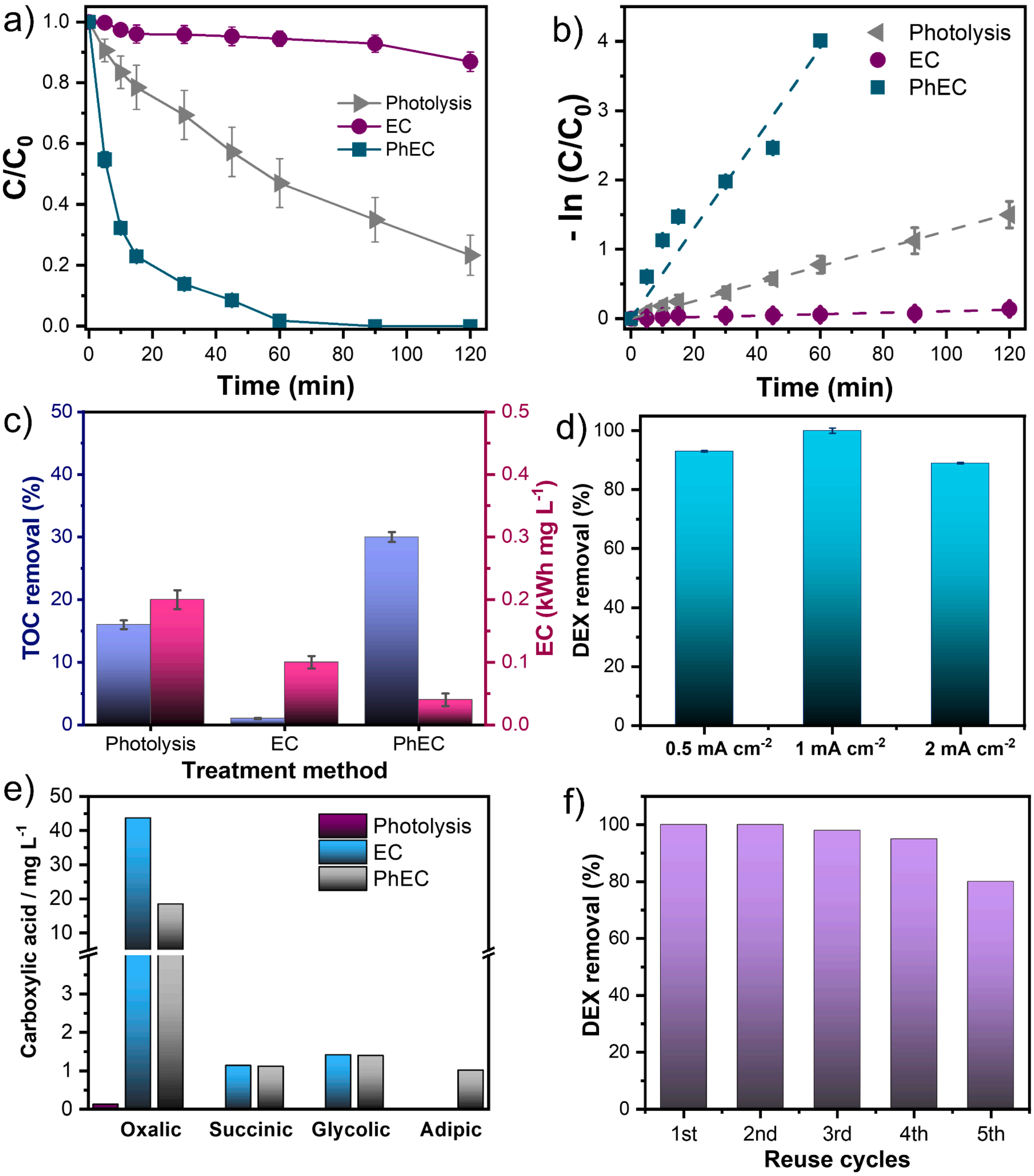

**Fig. 6.** (a) Dexamethasone removal at different treatment methods, including photolysis, electrocatalysis, and photoelectrocatalysis using $WO_3/BiVO_4$ electrode considering initial 10 mg $L^{-1}$ initial under simulated solar irradiation applying 1 mA cm$^{-2}$, (b) kinetics decay as a function of treatment time by different processes, (c) TOC removal DEX effluent simulation and energy consumption by different processes, (d) DEX removal at different current densities in 0.5 mol $L^{-1}$, (e) Obtained values for formed carboxylic acids, short term for the samples after 120 min photolysis, EC, and PhEC degradations applying 1 mA cm$^{-2}$, and (f) removal of DEX in five reuse cycles.

characterized by FE-SEM, EDS, and XPS. The FE-SEM image shows that the film before and after the application of DEX in PhEC (Fig. 7 (a-b)) did not present any explicit change in morphology. The corresponding EDS mapping of the W, Bi, V, and O elements of the used $WO_3/BiVO_4$ film demonstrated in Fig. 7(c) evidences the presence of all heterojunction elements throughout the electrode without contamination or removal of the film from the FTO substrate after PhEC. Fig. 7(d) presents the XPS survey spectrum of the $WO_3/BiVO_4$ electrode before and after the degradation cycles; it, is observed that a minimum amount of V and W may have been removed from the surface demonstrating a reduction of these peaks after PhEC [63], which may explain the slight reduction in degradation efficiency from the fourth to the fifth reuse cycle. Comparing the high-resolution spectra of W 4f, Bi 4f, V 2p, and O 1s (Fig. 7 (e-f)),a modification in the O 1s spectrum is observed after PhEC. A peak increase in the region from 534 to 529 eV is observed, indicating a high amount of surface adsorbed $H_2O$ ($H_2$Oads) on the $WO_3/BiVO_4$ surface. This change may occur after the application of current density in PhEC and modifications in pH, resulting in a decrease in lattice oxygen [64]. The adsorbed −OH groups on the metal oxide surface can be affected by ambient humidity, resulting in an apparent peak area increase at 532 eV of O 1s [65]. The characterization results of the $WO_3/BiVO_4$ heterojunction film after the PhEC process demonstrate the strength and quality of the prepared film, which does not lose its properties and presents minimal changes after PhEC. These are essential

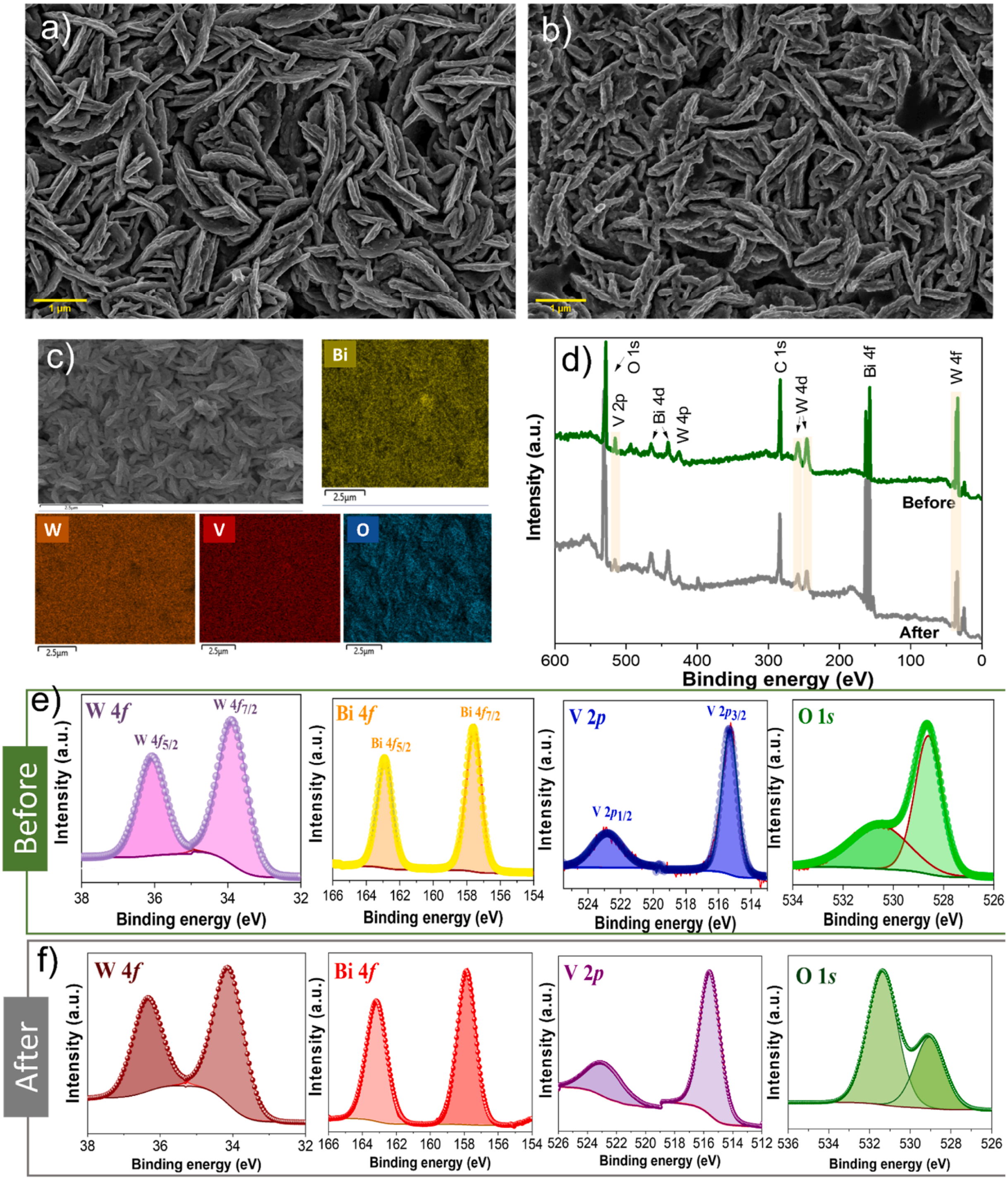

**Fig. 7.** SEM micrographs of the $WO_3/BiVO_4$ electrode before (a) and after (b) photoelectrodegradation, (c) EDS mapping $WO_3/BiVO_4$ electrode after photoelectrodegradation, (d) Survey spectrum comparison of before and after PhEC, and comparison of high-resolution spectra of W 4f, Bi 4f, V 2p, and O 1s before (e) and after (f) photoelectrodegradation of DEX.

characteristics for the service life of the proposed $WO_3/BiVO_4$ electrode and future applications of the material in more complex matrices.

### 3.5. *Toxicity and photoelectrocatalytic mechanism DEX removal*

After the oxidation process of recalcitrant organic compounds, the reaction intermediates and oxidation end products may become more hazardous than the original compounds. Reducing toxicity after effluent treatment is essential to achieve the actual application of photoelectrochemical technology. Usually, the removal of organic compounds is often evaluated. However, the toxicity assessment of the end products is not fully elucidated. In our studies, the toxicity evaluation before and after DEX treatment for different processes (photolysis, EC, and PhEC) was carried out using bioassays with *Lactuca sativa*, analyzing the germination index and root growth, following the methodology previously used by Doria et al. (2020) [66]. Fig. 8(a) shows the germination index (GI) and relative growth index (RGI) before and after treatment. According to the literature, the lower the GI value, the greater the toxicity of the medium. When analyzing the results of water (control) and DEX in the GI and RGI values, it is evident that a significant

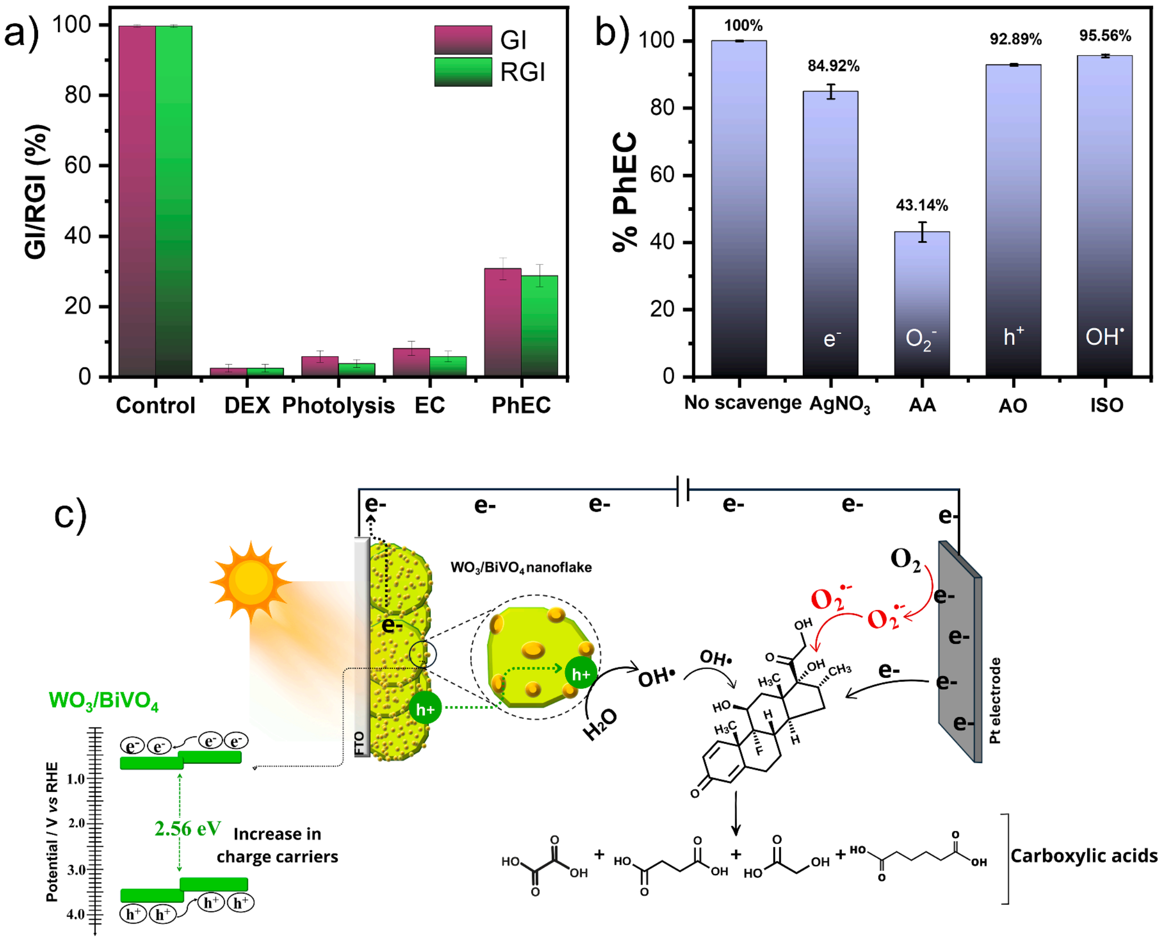

**Fig. 8.** (a) Relative growth index and germination index ( %), considering samples analyzed before and after 120 min in different photolysis, EC, and PhEC treatments in $Na_2SO_4$ 0.5 mol $L^{-1}$ applying 1 mA cm$^{-2}$, (b) the analysis of the effects of scavengers (5.0 mmol $L^{-1}$) on the PhEC of DEX for $^{\bullet}$OH (ISO), $h^{+}$ (AO), $^{\bullet}O_2^{-}$ (AA) and $e^{-}$ ($AgNO_3$), and (c) Schematic mechanism of DEX degradation on $BiVO_4/WO_3$ electrode surface under photoelectrocatalysis conditions.

difference exists. DEX is toxic to *Lactuca sativa*, with GI and RGI values of only 2 %. Compared to the photolysis and electrocatalysis processes, the GI and RGI values do not exceed 8 %, demonstrating that only applying light or a current density of 1 mA cm$^{-2}$ cannot reduce the anti-inflammatory's toxicity. These values agree with those presented in the degradation and TOC; therefore, although photolysis can degrade 76 % of DEX, its ineffectiveness in reducing toxicity at the end of 120 min is proven. However, PhEC reached a GI value of 31 % and RGI of 29 %, demonstrating a significant reduction in DEX toxicity compared to the initial DEX values of 2 %. This result corroborates the higher DEX removal rate observed previously, indicating a high efficiency of DEX degradation by applying $WO_3/BiVO_4$ film in PhEC since the higher the efficiency of the film in photoelectrocatalysis, the less drug will be present in the final effluent, reducing its toxicity. Therefore, determining the toxicity potential of a substance by measuring its response to a living organism through ecotoxicity tests enables the analysis of the possibility of reusing treated water for processes such as crop irrigation. Determining the detoxification capacity of the PhEC system proposed for treating real effluents is crucial [11,30,67].

For a better understanding of the degradation mechanism of DEX employing the $WO_3/BiVO_4$ electrode in the photoelectrocatalytic process, the trapping/quenching agents (also referred to as scavengers) capture $^{\bullet}$OH, $h^{+}$, $^{\bullet}O_2^{-}$ and $e^{-}$using ISO, AO, AA, and $AgNO_3$, respectively [68]. As observed in Fig. 7(b), the addition of ISO, AO, AA, and $AgNO_3$ in the reaction medium led to a decrease in DEX removal from 100 % to 95.6 %, 92.9 %, 43.14 %, and 84.92 %, respectively, which indicates that the species contributed differently to the degradation of DEX, with emphasis on the $^{\bullet}O_2^{-}$ radical. The scavenger experiments are quantitative. Therefore, the suppression effect of these species in the photocatalytic reaction is related to their oxidative capacity and radical chain reaction processes, which can alter the impact of these individual species [69]. The exceptional performance of $WO_3/BiVO_4$ for degrading DEX under PhEC conditions can be attributed to a combination of electrocatalysis and photocatalysis mechanisms. The applied current density (1 mA cm$^{-2}$) actively participates in the mass transfer of DEX species to the electrodes by electrostatic attraction and prevents the recombination of $h^{+}/e^{-}$ photogenerated by light irradiation. On the electrode surface, the $h^{+}$ generated contributes to the direct oxidation of DEX and can also generate $^{\bullet}$OH radicals that can indirectly attack some intermediate (Int) produced by DEX in the reaction medium and create products [57], as shown in Eqs. 7 – 10.

$$WO_3/BiVO_4 + h\nu \rightarrow \left(e^{-}{}_{CB}\right) + \left(h^{+}{}_{VB}\right) \tag{7}$$

$$h^{+}{}_{VB} + DEX \rightarrow oxidation\ of\ DEX \tag{8}$$

$$h^{+}{}_{VB} + H_2O \rightarrow H^{+} + \bullet OH \tag{9}$$

$$\bullet OH + DEX \rightarrow Int \tag{10}$$

At the cathode, the electrons conducted from the application of the current density can react with DEX and, as shown in Fig. 8(b), react directly with $O_2$ molecules to generate superoxide radicals ($^{\bullet}O_2^{-}$), which are the species that mainly contribute to the degradation, generation of intermediates and mineralization of a part of the DEX present in the reaction medium. These reactions are presented in Eqs. (11) - 14.

$$WO_3/BiVO_4 + current\ density \rightarrow external\ circuit \quad (11)$$

$$e^-_{CB} + O_2 \rightarrow \bullet O_2^- \quad (12)$$

$$\bullet O_2^- + DEX \rightarrow Int \rightarrow products \quad (13)$$

$$products \rightarrow CO_2 + H_2O \quad (14)$$

The significant contribution of the $^{\bullet}O_2^-$ radical in the DEX removal process may be related to the galvanostatic nature of the applied treatment, which promotes a large amount of $O_2$ in the photoanode. As shown by Fernandes et al. (2024) [70], who obtained similar results, the e-conducted by the external circuit after applying the current density reduced the $O_2$ in the reaction medium. Due to the large amount of $^{\bullet}O_2^-$ generated, the contribution of the other oxidative species generated in the PhEC process can be reduced. Based on the results presented above, an explanatory diagram of the PhEC activity of the $WO_3/BiVO_4$ electrode is shown in Fig. 8(c).

The results obtained in this work showed that the highest DEX removal rates were obtained in PhEC with $WO_3/BiVO_4$ in sodium sulfate solution with the application of 1 mA $cm^{-2}$ and visible irradiation. DEX is a recalcitrant compound occurring in wastewater. The $WO_3/BiVO_4$ electrode proved to be an excellent photocatalytic material in degrading the anti-inflammatory DEX under the conditions studied. This electrode is a versatile material, easy to obtain, and has good stability. Applying it and getting 100 % removal of the organic compound is possible. Furthermore, it is possible to work with $WO_3/BiVO_4$ under low current density conditions (1 mA $cm^{-2}$), which differentiates it from other photocatalyst materials used in the oxidation of organic compounds that generally require more extreme conditions and several hours for the complete oxidation of the molecule [71–73]. Another advantage PhEC proposed in treating water containing DEX is the degradation of organic intermediates formed during oxidation, forming short-chain acids and mineralizing part of the DEX, generating a treated residue with lower toxicity.

## 4. Conclusion

The following conclusions can be drawn from this work:

- In this work, the $WO_3/BiVO_4$ electrode was developed by combining simple steps, by chemical bath and spin coating, to obtain a heterojunction with improved light capture and charge transfer properties for application in the photoelectrochemical oxidation of DEX.
- -The evaluation of the electrochemical properties made it clear that the heterojunction achieved the lowest resistance to transfer and recombination of para $e^-/h^+$, as well as an increase of 3.3 and 25.9 times in charge carriers when compared to $WO_3$ and $BiVO_4$, surpassing the performance of the individual components.
- The results obtained from the degradation tests carried out in the study showed that the application of the $WO_3/BiVO_4$ electrode under PhEC led to a 100 % removal of DEX with 30 % mineralization compared to the photolysis and EC processes. Demonstrating the tremendous synergistic effect of combining light with electrode polarization in PhEC.
- Applying 1 mA $cm^{-2}$ in $WO_3/BiVO_4$ in PhEC led to the highest removal rates with lower energy consumption. The evaluation of five reuse cycles and the electrode analysis after degradation demonstrated the excellent stability and quality of the proposed electrode. The toxicity of the reaction products was elucidated by tests with *Lactuca sativa*, which proves the efficiency of PhEC by forming fewer toxic products than those obtained for the separate processes.
- By studying the action of the scavengers, the degradation process of DEX with PhEC was elucidated. The findings of the study showed that the application of PhEC led to the formation of different radical species, including $^{\bullet}O_2^-$ and $^{\bullet}OH$, as well as the $e^-/h^+$ pairs photogenerated on the electrode surface; this result points to the complex process involved in DEX degradation. These results point to the versatility of the $WO_3/BiVO_4$ electrode and the applicability of PhEC for the effective treatment of organic pollutants in other media, such as complex water matrices.

## CRediT authorship contribution statement

**Roberta Y.N. Reis:** Writing – original draft, Validation, Methodology, Investigation, Formal analysis, Data curation, Conceptualization. **Isabelle M.D. Gonzaga:** Writing – original draft, Validation, Resources, Formal analysis, Data curation, Conceptualization. **Roger Gonçalves:** Methodology, Investigation, Formal analysis, Conceptualization. **Carlos H.M. Fernandes:** Writing – original draft, Methodology, Investigation, Formal analysis. **Marcelo Assis:** Writing – original draft, Investigation, Formal analysis, Data curation. **Ernesto C. Pereira:** Visualization. **Marcos R.V. Lanza:** Visualization, Formal analysis. **Lucia H. Mascaro:** Writing – review & editing, Visualization, Supervision, Resources, Funding acquisition, Conceptualization.

## Declaration of competing interest

The authors declare that they have no known competing financial interests or personal relationships that could have appeared to influence the work reported in this paper.

## Acknowledgments

The authors thank Professor Valmor Mastelato for the XPS measures. Authors acknowledge the This study was financed, in part, by the São Paulo Research Foundation (FAPESP), Brazil. Process Number #2013/07296–2, #2017/11986–5, #2022/12895–1, #2018/22210–0, #2018/22211–7, #2018/22022–0, #2021/11326–0, #2020/15211–0, #2023/06558–5, 2023/08525-7 and #2024/20757–3). Coordenação de Aperfeiçoamento de Pessoal de Nível Superior - Brazil (CAPES). Conselho Nacional de Desenvolvimento Científico e Tecnológico (CNPq, grants #303943/2021–1, #152607/2022–6, #311769/2022–5, #406156/2022–0, #405733/2022–4 and #151171/2024–6). Financiadora de Estudos e Projetos FINEP grant number #01.22.0179.00. The authors also thank Shell for the strategic importance of the support given by ANP (Brazil's National Oil, Natural Gas, and Biofuels Agency) through the R&D levy regulation.

## Supplementary materials

Supplementary material associated with this article can be found, in the online version, at doi:10.1016/j.electacta.2025.146195.

## Data availability

Data will be made available on request.

## References

[1] A. Mukhopadhyay, S. Duttagupta, A. Mukherjee, Emerging organic contaminants in global community drinking water sources and supply: a review of occurrence, processes and remediation, J. Environ. Chem. Eng. 10 (2022), https://doi.org/10.1016/j.jece.2022.107560.

[2] H. Ramírez-Malule, D.H. Quiñones-Murillo, D. Manotas-Duque, Emerging contaminants as global environmental hazards. A bibliometric analysis, Emerg. Contam. 6 (2020), https://doi.org/10.1016/j.emcon.2020.05.001.

[3] L.A. Schaider, K.M. Rodgers, R.A. Rudel, Review of organic wastewater compound concentrations and removal in onsite wastewater treatment systems, Environ. Sci. Technol. 51 (2017), https://doi.org/10.1021/acs.est.6b04778.

[4] K. Jia, Q. Sheng, Y. Liu, Y. Yang, G. Dong, Z. Qiao, M. Wang, C. Sun, D. Han, A framework for achieving urban sustainable development goals (SDGs): evaluation and interaction, Sustain. Cities Soc. 114 (2024), https://doi.org/10.1016/j.scs.2024.105780.

[5] I. Nassri, S. khattabi rifi, F. Sayerh, S. Souabi, Occurrence, pollution sources, and mitigation prospects of antibiotics, anti-inflammatories, and endocrine disruptors in the aquatic environment, Environ. Nanotechnol. Monit. Manage. 20 (2023), https://doi.org/10.1016/j.enmm.2023.100878.

[6] A. Majumder, A.K. Gupta, P.S. Ghosal, M. Varma, A review on hospital wastewater treatment: a special emphasis on occurrence and removal of pharmaceutically active compounds, resistant microorganisms, and SARS-CoV-2, J. Environ. Chem. Eng. 9 (2021), https://doi.org/10.1016/j.jece.2020.104812.

[7] D. Mao, S. Yu, M. Rysz, Y. Luo, F. Yang, F. Li, J. Hou, Q. Mu, P.J.J. Alvarez, Prevalence and proliferation of antibiotic resistance genes in two municipal wastewater treatment plants, Water Res. 85 (2015), https://doi.org/10.1016/j.watres.2015.09.010.

[8] O.S. Arvaniti, A. Ioannidi, A. Politi, K. Miserli, I. Konstantinou, D. Mantzavinos, Z. Frontistis, Dexamethasone degradation in aqueous medium by a thermally activated persulfate system: kinetics and transformation products, J. Water Process Eng. 49 (2022), https://doi.org/10.1016/j.jwpe.2022.103134.

[9] J.A. Garrido-Cardenas, B. Esteban-García, A. Agüera, J.A. Sánchez-Pérez, F. Manzano-Agugliaro, Wastewater treatment by advanced oxidation process and their worldwide research trends, Int. J. Environ. Res. Public Health 17 (2020), https://doi.org/10.3390/ijerph17010170.

[10] I.A. Ricardo, E.A. Alberto, A.H. Silva Júnior, D.L.P. Macuvele, N. Padoin, C. Soares, H. Gracher Riella, M.C.V.M. Starling, A.G. Trovó, A critical review on microplastics, interaction with organic and inorganic pollutants, impacts and effectiveness of advanced oxidation processes applied for their removal from aqueous matrices, Chem. Eng. J. 424 (2021), https://doi.org/10.1016/j.cej.2021.130282.

[11] A.S. Lima, R.D.C. Rocha, E.C. Pereira, M. de S. Sikora, Photodegradation of ciprofloxacin antibiotic over TiO2 grown by PEO: ecotoxicity response in Lactuca sativa L. and Lemna minor, Int. J. Environ. Sci. Technol. 19 (2022), https://doi.org/10.1007/s13762-021-03239-9.

[12] B.A. Koiki, B.O. Orimolade, B.N. Zwane, O.V. Nkwachukwu, C. Muzenda, D. Nkosi, O.A. Arotiba, The application of FTO-Cu2O/Ag3PO4 heterojunction in the photoelectrochemical degradation of emerging pharmaceutical pollutant under visible light irradiation, Chemosphere 266 (2021) 129231, https://doi.org/10.1016/J.CHEMOSPHERE.2020.129231.

[13] R.Y.N. Reis, L.A. Goulart, L.H. Mascaro, S.A. Alves, A critical view of the contributions of photoelectrochemical technology to pharmaceutical degradation, J. Environ. Chem. Eng. 10 (2022) 107859, https://doi.org/10.1016/j.jece.2022.107859.

[14] G. Divyapriya, S. Singh, C.A. Martínez-Huitle, J. Scaria, A.v. Karim, P.v. Nidheesh, Treatment of real wastewater by photoelectrochemical methods: an overview, Chemosphere 276 (2021), https://doi.org/10.1016/j.chemosphere.2021.130188.

[15] K. Wetchakun, N. Wetchakun, S. Sakulsermsuk, An overview of solar/visible light-driven heterogeneous photocatalysis for water purification: tiO2- and ZnO-based photocatalysts used in suspension photoreactors, J. Indus. Eng. Chem. 71 (2019) 19–49, https://doi.org/10.1016/j.jiec.2018.11.025.

[16] X. Jiang, Q. Lin, M. Zhang, G. He, Z. Sun, Microstructure, optical properties, and catalytic performance of Cu2O-modified ZnO nanorods prepared by electrodeposition, Nanoscale Res. Lett. 10 (2015), https://doi.org/10.1186/s11671-015-0755-0.

[17] K.A. Agrafioti, N.T. Panagiotopoulos, C. Moularas, Y. Deligiannakis, C. Prouskas, P. P. Soukouli, G.A. Evangelakis, Development of Ti-based nanocomposite oxide thin films with CuO and Nb2O5 additions suitable for catalytic applications, Thin. Solid Films 775 (2023) 139864, https://doi.org/10.1016/J.TSF.2023.139864.

[18] T. Zhang, J. Liu, F. Zhou, S. Zhou, J. Wu, D. Chen, Q. Xu, J. Lu, Polymer-coated Fe2O3Nanoparticles for photocatalytic degradation of organic materials and antibiotics in water, ACS Appl. Nano Mater. 3 (2020), https://doi.org/10.1021/acsanm.0c01829.

[19] A.U.R. Bacha, I. Nabi, H. Cheng, K. Li, S. Ajmal, T. Wang, L. Zhang, Photoelectrocatalytic degradation of endocrine-disruptor bisphenol – A with significantly activated peroxymonosulfate by Co-BiVO4 photoanode, Chem. Eng. J. 389 (2020), https://doi.org/10.1016/j.cej.2020.124482.

[20] D. Liu, H. Li, R. Gao, Q. Zhao, Z. Yang, X. Gao, Z. Wang, F. Zhang, W. Wu, Enhanced visible light photoelectrocatalytic degradation of tetracycline hydrochloride by I and P co-doped TiO2 photoelectrode, J. Hazard. Mater. 406 (2021), https://doi.org/10.1016/j.jhazmat.2020.124309.

[21] M. Liu, Y. Wan, Y. Wang, J. Xu, X. Li, Robust photoelectrocatalytic degradation of antibiotics by organic-inorganic PDISA/Bi2WO6 S-scheme heterojunction membrane, J. Environ. Chem. Eng. 12 (2024), https://doi.org/10.1016/j.jece.2024.112328.

[22] Z. Chi, J. Zhao, Y. Zhang, H. Yu, H. Yu, Coral-like WO3/BiVO4 photoanode constructed via morphology and facet engineering for antibiotic wastewater detoxification and hydrogen recovery, Chem. Eng. J. 428 (2022) 131817, https://doi.org/10.1016/J.CEJ.2021.131817.

[23] M. Pedroni, G.L. Chiarello, E. Vassallo, E. Selli, Multilayer WO3/BiVO4 photoanodes for solar-driven water splitting prepared by RF-plasma sputtering, Surfaces 3 (2020), https://doi.org/10.3390/surfaces3010010.

[24] N. Omrani, A. Nezamzadeh-Ejhieh, BiVO4/WO3 nano-composite: characterization and designing the experiments in photodegradation of sulfasalazine, Environ. Sci. Pollut. Res. 27 (2020) 44292–44305, https://doi.org/10.1007/s11356-020-10278-1.

[25] W. Zhang, M. Tian, H. Jiao, H.Y. Jiang, J. Tang, Conformal BiVO4/WO3 nanobowl array photoanode for efficient photoelectrochemical water splitting, Chin. J. Cataly. 43 (2022) 2321–2331, https://doi.org/10.1016/S1872-2067(21)63927-X.

[26] L. Cheng, T. Jiang, J. Zhang, Photoelectrocatalytic degradation of deoxynivalenol on CuO-Cu2O/WO3 ternary film: mechanism and reaction pathways, Sci. Total Environ. 776 (2021), https://doi.org/10.1016/j.scitotenv.2021.145840.

[27] F.W.P. Ribeiro, M.F. Gromboni, F. Marken, L.H. Mascaro, Photoelectrocatalytic properties of BiVO4 prepared with different alcohol solvents, Int. J. Hydrogen Energy 41 (2016) 17380–17389, https://doi.org/10.1016/J.IJHYDENE.2016.07.159.

[28] C.H.M. Fernandes, B.F. Silva, J.M. Aquino, On the performance of distinct electrochemical and solar-based advanced oxidation processes to mineralize the insecticide imidacloprid, Chemosphere 275 (2021) 130010, https://doi.org/10.1016/J.CHEMOSPHERE.2021.130010.

[29] S. Cotillas, M.J.M. de Vidales, J. Llanos, C. Sáez, P. Cañizares, M.A. Rodrigo, Electrolytic and electro-irradiated processes with diamond anodes for the oxidation of persistent pollutants and disinfection of urban treated wastewater, J. Hazard. Mater. 319 (2016) 93–101, https://doi.org/10.1016/J.JHAZMAT.2016.01.050.

[30] M. Assis, J.S. da Silva, M.O. Gonçalves, J.M. de Almeida Rodolpho, B.D. de Lima Fragelli, A.B.P. Corte, L.K. Ribeiro, M.D. Teodoro, F. de Freitas Anibal, C.P. de Sousa, O.N. Oliveira, J. Andrés, E. Longo, Bactericidal activity of Ag4V2O7/β-AgVO3 heterostructures against antibiotic-resistant Klebsiella pneumoniae, Biomater. Adv. 141 (2022) 213097, https://doi.org/10.1016/J.BIOADV.2022.213097.

[31] L. Kong, X. Guo, J. Xu, Z. Mo, L. Li, Morphology control of WO3 nanoplate film on W foil by oxalic acid for photocatalytic gaseous acetaldehyde degradation, J. Photochem. Photobiol. a Chem. 401 (2020), https://doi.org/10.1016/j.jphotochem.2020.112760.

[32] Q. Zeng, J. Li, J. Bai, X. Li, L. Xia, B. Zhou, Preparation of vertically aligned WO3 nanoplate array films based on peroxotungstate reduction reaction and their excellent photoelectrocatalytic performance, Appl. Catal. B 202 (2017) 388–396, https://doi.org/10.1016/j.apcatb.2016.09.045.

[33] N. Le Minh Tri, N.T.D. Cam, H.D. Pham, D. Van Thuan, T.D. Pham, V.T. Nguyen, N. T. Trung, M.H.T. Tung, T.T.T. Phuong, T.T.P. Nguyen, C. Van Hoang, V.D. Dao, Development of g-C3N4/BiVO4 binary component heterojunction as an advanced visible light-responded photocatalyst for polluted antibiotics degradation, Top. Catal. 63 (2020), https://doi.org/10.1007/s11244-020-01368-y.

[34] A.E.B. Lima, M. Assis, A.L.S. Resende, H.L.S. Santos, L.H. Mascaro, E. Longo, R. S. Santos, L.S. Cavalcante, G.E. Luz, CuWO4|MnWO4 heterojunction thin film with improved photoelectrochemical and photocatalytic properties using simulated solar irradiation, J. Solid State Electrochem. 26 (2022) 997–1011, https://doi.org/10.1007/s10008-022-05143-9.

[35] M.G. Guardiano, L.K. Ribeiro, I.M.D. Gonzaga, L.H. Mascaro, Effect of cerium precursors on Ce-doped BiVO4 nanoscale-thick films as photoanodes: implications for water splitting, ACS Appl. Nano Mater. (2024), https://doi.org/10.1021/acsanm.4c03537.

[36] M.A. Mahadik, I.S. Hwang, W.S. Chae, H.H. Lee, S.H. Choi, M. Cho, J.S. Jang, Synergistic role of hydrogen treatment and heterojunction in H-WO3-x/TiO2-x NT/Ti foil-based photoanodes for photoelectrochemical wastewater detoxification and antibacterial activity, Chemosphere 318 (2023), https://doi.org/10.1016/j.chemosphere.2023.137973.

[37] A. Aranda-Aguirre, J.M. de Oca, A. Corzo, S. Garcia-Segura, H. Alarcon, Mixed metal oxide Bi2O3/Bi2WO6 thin films for the photoelectrocatalytic degradation of histamine, J. Electroanaly. Chem. 919 (2022) 116528, https://doi.org/10.1016/J.JELECHEM.2022.116528.

[38] A.K. Thakur, M.V. Limaye, S. Rakshit, K.N. Maity, V. Gupta, P.K. Sharma, S. B. Singh, Controlled synthesis of WO3 nanostructures: optical, structural and electrochemical properties, Mater. Res. Express 6 (2019), https://doi.org/10.1088/2053-1591/aae991.

[39] C. Yin, S. Zhu, D. Zhang, 3D nanostructured WO3/BiVO4 heterojunction derived from Papilio Paris for efficient water splitting, RSC Adv. 7 (2017) 27354–27360, https://doi.org/10.1039/c7ra03491a.

[40] V. Uskoković, Toward functionalization without functional agents: an X-ray photoelectron spectroscopy study, Colloids Surf. a Physicochem. Eng. Asp. 651 (2022), https://doi.org/10.1016/j.colsurfa.2022.129676.

[41] X. Zhang, X. Wang, D. Wang, J. Ye, Conformal BiVO 4 -layer/WO 3 -nanoplate-array heterojunction photoanode modified with cobalt phosphate cocatalyst for significantly enhanced photoelectrochemical performances, ACS Appl. Mater. Interf. 11 (2019), https://doi.org/10.1021/acsami.8b05477.

[42] S. Santhosh, K. Balamurugan, M. Mathankumar, K. Shankar, B. Subramanian, Electrochromic and optical studies on Nb2O5–NiO mixed oxide films for smart window applications, Opt. Mater. (Amst) 135 (2023) 113248, https://doi.org/10.1016/J.OPTMAT.2022.113248.

[43] L.H. Mascaro, H. Santos, Enhanced photoelectrochemical water splitting using nanostructured films: p-CuO sensitized with polyhedral n-Cu2O particles and CuS as photocathode, Mater. Adv. (2024), https://doi.org/10.1039/d4ma00343h.

[44] P. Makuła, M. Pacia, W. Macyk, How to correctly determine the band gap energy of modified semiconductor photocatalysts based on UV-vis spectra, J. Phys. Chem. Lett. 9 (2018), https://doi.org/10.1021/acs.jpclett.8b02892.

[45] J. Su, T. Zhang, L. Wang, Engineered WO3 nanorods for conformal growth of WO3/BiVO4 core–shell heterojunction towards efficient photoelectrochemical water oxidation, J. Mater. Sci.: Mater. Electron. 28 (2017), https://doi.org/10.1007/s10854-016-6082-0.

[46] M.A. Khalifa, L. Shen, J. Zheng, C. Xu, Boosting light harvesting and charge separation of WO3viacoupling with Cu2O/CuO towards highly efficient tandem photoanodes, RSC Adv. 11 (2021) 13513–13520, https://doi.org/10.1039/d1ra00417d.

[47] D. Coelho, J.P.R.S. Gaudêncio, S.A. Carminati, F.W.P. Ribeiro, A.F. Nogueira, L. H. Mascaro, Bi electrodeposition on WO3 photoanode to improve the photoactivity

of the WO3/BiVO4 heterostructure to water splitting, Chem. Eng. J. 399 (2020) 125836, https://doi.org/10.1016/J.CEJ.2020.125836.

[48] A.E.B. Lima, M.J.S. Costa, R.S. Santos, N.C. Batista, L.S. Cavalcante, E. Longo, G. E. Luz, Facile preparation of CuWO4 porous films and their photoelectrochemical properties, Electrochim. Acta 256 (2017) 139–145, https://doi.org/10.1016/j.electacta.2017.10.010.

[49] P. Muthukumar Sathya, S. Vadivel, T. Shin, H. Mohan, BiVO4@WO3 S-scheme nanocomposite for visible light photocatalytic CO2 reduction, Inorg. Chem. Commun. 144 (2022), https://doi.org/10.1016/j.inoche.2022.109924.

[50] T. Feng, F.K. Yam, The influence of hydrothermal treatment on TiO2 nanostructure films transformed from titanates and their photoelectrochemical water splitting properties, Surf. Interf. 38 (2023) 102767, https://doi.org/10.1016/J.SURFIN.2023.102767.

[51] M. Baitimirova, A. Osite, J. Katkevich, A. Viksna, Electrochemical characteristics of particulate matter, Environ. Climate Technol. 7 (2011), https://doi.org/10.2478/v10145-011-0023-1.

[52] K. Sivula, Mott-schottky analysis of photoelectrodes: sanity checks are needed, ACS Energy Lett. 6 (2021), https://doi.org/10.1021/acsenergylett.1c01245.

[53] C.C. Chen, Characterization of porous WO3 electrochromic device by electrochemical impedance spectroscopy, J. Nanomater. 2013 (2013), https://doi.org/10.1155/2013/785023.

[54] F. Amano, S. Koga, Electrochemical impedance spectroscopy of WO3 photoanodes on different conductive substrates: the interfacial charge transport between semiconductor particles and Ti surface, J. Electroanaly. Chem. 921 (2022), https://doi.org/10.1016/j.jelechem.2022.116685.

[55] K. Fujii, III-nitride semiconductor photoelectrodes, Semiconduc. Semimet. 97 (2017) 139–183, https://doi.org/10.1016/BS.SEMSEM.2017.03.003.

[56] J.M. Thornton, D. Raftery, Efficient photocatalytic hydrogen production by platinum-loaded carbon-doped cadmium indate nanoparticles, ACS Appl. Mater. Interf. 4 (2012), https://doi.org/10.1021/am300093t.

[57] L.A. Goulart, A. Moratalla, M.R.V. Lanza, C. Sáez, M.A. Rodrigo, Photoelectrocatalytic treatment of levofloxacin using Ti/MMO/ZnO electrode, Chemosphere 284 (2021), https://doi.org/10.1016/j.chemosphere.2021.131303.

[58] A.V. Quaresma, K.T.S. Rubio, J.G. Taylor, B.A. Sousa, S.Q. Silva, A.A. Werle, R.J.C. F. Afonso, Removal of dexamethasone by oxidative processes: structural characterization of degradation products and estimation of the toxicity, J. Environ. Chem. Eng. 9 (2021), https://doi.org/10.1016/j.jece.2021.106884.

[59] G.O.S. Santos, K.I.B. Eguiluz, G.R. Salazar-Banda, C. Saez, M.A. Rodrigo, Photoelectrolysis of clopyralid wastes with a novel laser-prepared MMO-RuO2TiO2 anode, Chemosphere 244 (2020) 125455, https://doi.org/10.1016/J.CHEMOSPHERE.2019.125455.

[60] I.M.D. Gonzaga, R. Gonçalves, C.H.M. Fernandes, M. Assis, I.F. Teixeira, L. H. Mascaro, Efficient photoelectrochemical real textile wastewater detoxification using photoanodes of C3N4–BiVO4, Chemosphere 352 (2024), https://doi.org/10.1016/j.chemosphere.2024.141315.

[61] S. Garcia-Segura, E. Brillas, Applied photoelectrocatalysis on the degradation of organic pollutants in wastewaters, J. Photochem. Photobiol. C: Photochem. Rev. 31 (2017) 1–35, https://doi.org/10.1016/J.JPHOTOCHEMREV.2017.01.005.

[62] G.O.S. Santos, I.M.D. Gonzaga, K.I.B. Eguiluz, G.R. Salazar-Banda, C. Saez, M. A. Rodrigo, Improving biodegradability of clopyralid wastes by photoelectrolysis: the role of the anode material, J. Electroanaly. Chem. 864 (2020) 114084, https://doi.org/10.1016/J.JELECHEM.2020.114084.

[63] Y. Shi, Y. Yu, Y. Yu, Y. Huang, B. Zhao, B. Zhang, Boosting photoelectrochemical water oxidation activity and stability of Mo-doped BiVO4 through the uniform assembly coating of NiFe-phenolic networks, ACS Energy Lett. 3 (2018), https://doi.org/10.1021/acsenergylett.8b00855.

[64] K. Fan, H. Zou, Y. Lu, H. Chen, F. Li, J. Liu, L. Sun, L. Tong, M.F. Toney, M. Sui, J. Yu, Direct observation of structural evolution of metal chalcogenide in electrocatalytic water oxidation, ACS Nano 12 (2018), https://doi.org/10.1021/acsnano.8b06312.

[65] Z. Wang, R. Lin, Y. Huo, H. Li, L. Wang, Formation, detection, and function of oxygen vacancy in metal oxides for solar energy conversion, Adv. Funct. Mater. 32 (2022), https://doi.org/10.1002/adfm.202109503.

[66] A.R. Dória, M. Pupo, G. de O.S. Santos, D. da S. Vilar, N.H. Torres, L.F. Romanholo Ferreira, E.B. Cavalcanti, K.I.B. Eguiluz, G.R. Salazar-Banda, Electrochemical oxidation of indanthrene blue dye in a filter-press flow reactor and toxicity analyses with Raphidocelis subcapitata and Lactuca sativa, Ecotoxicol. Environ. Saf. 198 (2020), https://doi.org/10.1016/j.ecoenv.2020.110659.

[67] A.R. Dória, R.S. Silva, P.H. Oliveira Júnior, E.A. dos Santos, S. Mattedi, P. Hammer, G.R. Salazar-Banda, K.I.B. Eguiluz, Influence of the RuO2 layer thickness on the physical and electrochemical properties of anodes synthesized by the ionic liquid method, Electrochim. Acta 354 (2020), https://doi.org/10.1016/j.electacta.2020.136625.

[68] M.L. Barbosa, M.J.S. Costa, A.E.B. Lima, A.M. Batista, E. Longo, L.S. Cavalcante, R. S. Santos, Anionic and cationic dyes removal by degradation via photoelectrocatalysis using a WO3/CuWO4 heterojunction film as a photoanode, Nano-Struct. Nano-Obj. 35 (2023), https://doi.org/10.1016/j.nanoso.2023.100993.

[69] B. Yuan, J. Wu, N. Qin, E. Lin, Z. Kang, D. Bao, Sm-doped $Pb(Mg_{1/3}Nb_{2/3})O_3$-$x$$PbTiO_3$ piezocatalyst: exploring the relationship between piezoelectric property and piezocatalytic activity, Appl. Mater. Today 17 (2019), https://doi.org/10.1016/j.apmt.2019.07.015.

[70] C.H.M. Fernandes, L.A. Goulart, R. Gonçalves, G.O.S. Santos, M.V.B. Zanoni, L. H. Mascaro, M.R.V. Lanza, Effective photoelectrocatalysis of levofloxacin antibiotic with Ti/IrO2[sbnd]Nb2O5 in environmental samples, Electrochim. Acta 475 (2024), https://doi.org/10.1016/j.electacta.2023.143586.

[71] E. Grilla, M.E. Taheri, K. Miserli, D. Venieri, I. Konstantinou, D. Mantzavinos, Degradation of dexamethasone in water using BDD anodic oxidation and persulfate: reaction kinetics and pathways, J. Chem. Technol. Biotechnol. 96 (2021), https://doi.org/10.1002/jctb.6833.

[72] P.J. Mafa, M.E. Malefane, F. Opoku, B.B. Mamba, A.T. Kuvarega, Visible light responsive MoS2/Ag@WO3/EG photoanode with highly stable Z-scheme induced circular electron motion pioneered by exfoliated graphite for bisphenol a photoelectrodegradation, Chem. Eng. J. 464 (2023), https://doi.org/10.1016/j.cej.2023.142462.

[73] C.A.G. Bezerra, J.P.T. da S. Santos, G.G. Bessegato, C.L. de Paiva e Silva Zanta, V. Del Colle, G. Tremiliosi-Filho, Photo- and electro-oxidation of tetracycline hydrochloride on self-doped titanium dioxide nanotubes modified by Pt sub-monolayers, Electrochim. Acta 404 (2022), https://doi.org/10.1016/j.electacta.2021.139712.